https://doi.org/10.5194/tc-2020-19
Preprint. Discussion started: 24 January 2020

The Cryosphere Discussions

Wave–sea-ice interactions in a brittle rheological framework

Guillaume Boutin[1], Timothy Williams[1], Pierre Rampal[1], Einar Olason[1], and Camille Lique[2]

[1]Nansen Environmental and Remote Sensing Center, Bergen, Norway
[2]Univ. Brest, CNRS, IRD, Ifremer, Laboratoire d'Océanographie Physique et Spatiale (LOPS), IUEM, Brest 29280, France

Correspondence: Guillaume Boutin (Guillaume.boutin@nersc.no)

Abstract. The decrease in Arctic sea ice extent is associated with an increase of the area where sea ice and open ocean interact, commonly referred to as the Marginal Ice Zone (MIZ). In this area, sea ice is particularly exposed to waves that can penetrate over tens to hundreds of kilometres into the ice cover. Waves are known to play a major role in the fragmentation of sea ice in the MIZ, and the interactions between wave-induced sea ice fragmentation and lateral melting have received particular attention in recent years. The impact of this fragmentation on sea ice dynamics, however, remains mostly unknown, although it is thought that fragmented sea ice experiences less resistance to deformation than pack ice. Here, we introduce a new coupled framework involving the spectral wave model WAVEWATCH III and the sea ice model neXtSIM, which includes a Maxwell-Elasto Brittle rheology. We use this coupled modelling system to investigate the potential impact of wave-induced sea ice fragmentation on sea ice dynamics. Focusing on the Barents Sea, we find that the decrease of the internal stress of sea ice resulting from its fragmentation by waves results in a more dynamical MIZ, in particular in areas where sea ice is compact. Sea ice drift is enhanced for both on-ice and off-ice wind conditions. Our results stress the importance of considering wave–sea-ice interactions for forecast applications. They also suggest that waves likely modulate the area of sea ice that is advected away from the pack by ocean (sub-)mesoscale eddies near the ice edge, potentially contributing to the observed past, current and future sea ice cover decline in the Arctic.

1 Introduction

The interactions between ocean surface waves and sea ice have been receiving a significant amount of attention in recent years, particularly motivated by the decreasing Arctic sea ice extent (Meier, 2017) resulting in larger areas of open water exposed to the wind and thus available for wave generation. As a consequence, wave events in the Arctic are expected to be more frequent and more intense (Thomson and Rogers, 2014), with waves penetrating far into the ice cover, and breaking large sea ice plates into floes of less than a few hundred metres (see e.g. Langhorne et al., 1998; Collins et al., 2015). The attenuation of waves by sea ice, however, limits this fragmentation to the interface between the open ocean and the pack ice, in the so-called Marginal Ice Zone (MIZ). The MIZ is a highly dynamic area characterized by strong interactions between the ocean, sea ice and atmosphere. State-of-the-art sea ice models used in climate prediction systems have been shown to fail at representing the complexity of these interactions, having their biggest errors in the MIZ (Tietsche et al., 2014). On shorter time-scales, large uncertainties remain in the forecasts of the position of the sea ice edge (Lemieux et al., 2016), whereas this information is essential for the safety of the increasing number of human activities in polar regions (Azzara et al., 2015). These inaccuracies

https://doi.org/10.5194/tc-2020-19
Preprint. Discussion started: 24 January 2020


The Cryosphere Discussions

can certainly be attributed (at least in part) to the lack of representation of some of the processes occurring in the MIZ, and the impact of the waves on sea ice dynamics is one of them.

There are two main processes through which waves can impact sea ice dynamics in the MIZ: by transferring momentum through what is called the wave radiative stress (WRS), and by changing the mechanical properties of the ice through fragmentation. The WRS corresponds to the momentum transferred by waves to sea ice during wave attenuation (Longuet-Higgins, 1977). It acts as a force that pushes the sea ice in the direction of the incident waves. Estimating wave attenuation from SAR images, Stopa et al. (2018b) estimated it to be as important as the wind stress over the first 50 km of the MIZ in the Southern Ocean. Being mostly directed on-ice, its main effect is to maintain a compact ice edge. The effect of sea ice fragmentation on sea ice dynamics is, as mentioned before, less clear. Intuitively, we expect that broken ice will be more mobile than continuous ice (e.g McPhee, 1980), having lower internal stress. This seems to be consistent with the deformation observations of Oikkonen et al. (2017) collected by ship radar during the N-ICE-2015 expedition. In their observations, deformation in fragmented sea ice was an order of magnitude higher than in the pack. However, in the absence of routinely available datasets providing synoptic information on sea ice drift, wave height, and floe size in the MIZ, observations do not allow us to conclude on any explicit relationship between the level of fragmentation and the ability of sea ice cover to be deformed.

A few attempts have been made to relate fragmentation to sea ice dynamics in theoretical models. Shen et al. (1986) used a collisional stress term accounting for floe size to represent sea ice behaviour in the MIZ. The fluctuations of the velocity field they obtain, however, did not reproduce observations from the MIZEX campaigns, being too small by an order of magnitude. Feltham (2005) uses a similar collisional stress but allows the velocity fluctuations to be time-dependent. He shows that it enables the generation of ice jets in the MIZ, but on smaller scales than the reported observations of ice jets by Johannessen et al. (1983). For these models also, the little amount of available observations in the MIZ makes any evaluation attempt very difficult. Nevertheless, recent developments focusing on wave–sea-ice interactions in both wave and sea ice models have still made it possible to take a fresh look at what could be the effects of lowering the internal stress of sea ice after it has been fragmented by waves.

Modelling efforts relating to waves-in-ice have made wave models progress a lot in recent years. Large arrays of floes have been modelled in order to represent multiple scattering (Montiel and Squire, 2017), while other studies focused on dissipative mechanisms (e.g Mosig et al., 2015; Ardhuin et al., 2016; Stopa et al., 2016; Cheng et al., 2017). A sequence of reviews by Squire et al. (1995) and Squire (2007, 2012, 2020) gives a more detailed history of this area of work. The interactions between waves and floe size, through the wave-induced sea ice fragmentation, have been particularly investigated, initially with one-dimensional studies looking at the feedback between ice breakup and wave attenuation (Dumont et al., 2011; Williams et al., 2013a, b). These models assume that the Floe Size Distribution (FSD) follows a truncated power-law, with its upper-limit (often called maximum floe size, $D_{\max}$) depending of the wave field (Dumont et al., 2011). This assumption on the shape of the FSD is based on the observations by Toyota et al. (2011) of power-law FSD in the MIZ that they explain by successive fragmentation of floes by waves. More recently, Boutin et al. (2018) included a parameterization in the spectral wave model WAVEWATCH III (WW3: The WAVEWATCH III Development Group, 2019), also assuming a power-law FSD. Their parameterization enables interactions between sea ice floe size and wave attenuation processes like scattering and inelastic dissipation. Ardhuin et al.

https://doi.org/10.5194/tc-2020-19
Preprint. Discussion started: 24 January 2020

(2018) evaluated this model by comparing their results to remote sensing and field measurements during a storm event in the Beaufort Sea, showing good agreement for the measured and modelled wave-in-ice attenuation and broken sea ice extent.

Large scale sea-ice models have also included parameterizations of wave-ice interactions. Zhang et al. (2015) proposed a model for the evolution of the full FSD driven by thermodynamical and dynamical processes. In parallel, Horvat and Tziperman (2015) proposed a model for the evolution of the combined ice thickness and floe size distribution (ITFSD). In both studies, the fragmentation of sea ice by waves is associated with a redistribution of the FSD/ITFSD. Bennetts et al. (2017) and Bateson et al. (2019) also implemented FSDs in the sea ice model CICE (Community Sea Ice Model), but using the same assumption as in the wave models described above: their FSD only depends on the wave field, assuming a truncated power-law distribution with an upper limit $D_{\max}$ evolving with the sea state. Coupling the wave model WW3 with the ocean-sea ice model NEMO-LIM3 (Rousset et al., 2015), Boutin et al. (2019) used the FSD approach suggested by Zhang et al. (2015) but combined it with a redistribution of the FSD after fragmentation by waves, leading to a truncated power-law similar to the one assumed by Bennetts et al. (2017) and Bateson et al. (2019).

These implementations of FSD/ITFSDs in sea ice models have been mostly used to investigate the effects of lateral melting on sea ice properties over timescales of a few weeks to a few years, in a context where lateral melt is expected to be enhanced by the wave-induced sea ice fragmentation (Asplin et al., 2012). Zhang et al. (2016) included the FSD model of Zhang et al. (2015) in the PIOMAS (Pan-Arctic Ice–Ocean Modeling and Assimilation System) ice-ocean model, while Roach et al. (2018) included the ITFSD model of Horvat and Tziperman (2015) into CICE coupled to the ocean model NEMO (Madec, 2008). All these studies find that lateral melt is very sensitive to the FSD, with the actual impact on sea ice concentration and thickness depending on the region. Roach et al. (2018), Boutin et al. (2019) and Bateson et al. (2019) also noticed that sea ice loss/gain due to changes in the lateral melt are mostly compensated by opposite variations of the bottom (or basal) melt.

The dynamical aspects of wave-ice interactions has received less attention in these models. Still using the truncated power-law assumption, Williams et al. (2017) used neXtSIM (neXt generation Sea Ice Model, Rampal et al., 2019), in a stand-alone set-up, to investigate the compressive effect of the wave radiative stress (WRS) on the sea ice edge. Boutin et al. (2019) also integrated the WRS in their wave–sea-ice–ocean framework, and found that its effect on sea ice drift has a regional impact on sea ice melt and sea surface properties in the Arctic MIZ at the end of summer. The study of Williams et al. (2017) also investigated the effect of reducing the internal stress of sea ice when it has been broken by waves, thus linking directly wave-induced fragmentation and sea ice dynamics. They proceeded by using a new state variable for sea ice introduced in neXtSIM, called damage, which considers and keeps track of the level of mechanical damage of the sea ice over each grid cell (Rampal et al., 2016). Using idealized simulations they showed that the movement of the ice edge was actually not very sensitive to either wave fragmentation or the WRS. However, neXtSIM is now including a Maxwell Elasto-Brittle (MEB) rheology (Dansereau et al., 2016) different from the Elasto-Brittle rheology (EB, Girard et al., 2011) used by Williams et al. (2017).

In this paper, we present results obtained with a new coupled wave–sea-ice modelling system (WW3-neXtSIM). This modelling system benefits from recent wave-ice developments in WW3 (Ardhuin et al., 2016; Boutin et al., 2018; Ardhuin et al., 2018) and extends the work done by Williams et al. (2017) in neXtSIM. We again use the damage variable to link the sea ice dynamics and the fragmentation due to waves, allowing us to represent the link between the wave-induced fragmentation of

https://doi.org/10.5194/tc-2020-19
Preprint. Discussion started: 24 January 2020

sea ice and its mobility in MIZ areas. It also benefits from the advancements of FSD implementations in sea ice models done by Zhang et al. (2015) and Horvat and Tziperman (2015), and of the coupling of WW3 with the sea ice model LIM3 described by Boutin et al. (2019). Since there are reports of waves breaking ice at weak points such as refrozen cracks and pressure ridges (eg. Kohout et al., 2016), we also propose a way to incorporate some memory of previous events of sea ice break-up due to waves. To do so, we introduce two time-evolving FSDs in each grid cell, each FSD being associated with a different timescale depending on the processes it is associated with. The first FSD is driven by the sea ice mechanics and the second, more classical, driven by thermodynamics (as in e.g. Roach et al., 2018). These developments provide a coupled wave–sea-ice framework able to provide all-year-round regional or pan-Arctic simulations. After describing the details of our implementation, we evaluate our new coupled framework to check that the produced wave attenuation, broken sea ice extent, and refreezing timescales are reasonable. We then investigate the effects of wave-induced sea ice fragmentation using a regional case study. Finally, we discuss the different assumptions made in our study, and suggest perspectives for future studies.

2 Implementation of the coupling between the wave and sea ice models

In this study we make use of the spectral wave model WAVEWATCH III® (The WAVEWATCH III Development Group, 2019), building on the previous developments performed by Boutin et al. (2018) who included an FSD in WW3 as well as some representations of the different processes by which sea ice can affect the propagation and modulation of waves in the MIZ. These processes are scattering (which redistributes the wave energy without dissipation), friction under sea ice (with a viscous and a turbulent part depending on the wave Reynolds number), and inelastic flexion. All these processes depend on sea ice thickness, concentration, and floe size. We also use the sea ice model neXtSIM (Rampal et al., 2019), in which an FSD is first implemented as described in Section 2.2. The two models are coupled through the coupler OASIS-MCT (Craig et al., 2017). Figure 1 shows the variables that are exchanged. To give a brief summary: WW3 determines if the waves will break the ice and calculates a representative wavelength λ_{break} in the manner of Boutin et al. (2018). This is then used by neXtSIM to modify the FSD as described below in Section 2.2.2. WW3 also computes the WRS which is used in the momentum equation of neXtSIM. neXtSIM gives WW3 the sea ice concentration and thickness, and the mean and maximum floe size, which are used by WW3 to determine the amount of attenuation. The mean floe size is used to determine the amount of scattering, while the maximum floe size is used to determine the amount of dissipation due to inelastic attenuation. The evolution of the FSD and the computation of the exchanged variables are described in more details in the following paragraphs.

2.1 Wave radiative stress on sea ice

As in Boutin et al. (2019), the WRS is computed in WW3 and sent to the ice model. The WRS in neXtSIM is added to the sea ice momentum equation in the same way as in Williams et al. (2017) study, although the sea ice rheology in this paper is different - we are using the MEB rheology, whereas that paper used the EB rheology.

https://doi.org/10.5194/tc-2020-19
Preprint. Discussion started: 24 January 2020


The Cryosphere Discussions

2.2 Floe size distribution modelling

As mentioned in the introduction, this study makes use of two different FSDs to represent the evolution of the floe size. The idea of evolving two FSDs comes from the different timescales involved in the sea ice thermodynamics and mechanics. For instance, floe welding and freezing occurring in leads can transform a fragmented sea ice cover into a continuous one in a few hours to a few days, depending on the compactness of the ice. From an aerial photography of these freshly jointed floes, one could conclude that the sea ice cover is almost continuous, or at least made of large plates, especially if the ice is recovered by snow. In melting conditions, lateral melt is likely to be negligible compared to basal melt (Steele, 1992). An observer located on the sea ice cover would, however, find a heterogeneous gathering of consolidated floes jointed by a more fragile sea ice layer. In case of any new fragmentation events, it is expected that these not-yet-consolidated joints would quickly fail, re-activating the fractures created by a previous event. This is coherent with the observation of Kohout et al. (2016), for example, which report a fragmentation event with cracks clearly opening at pre-existing ridges and weak points, advocating for the need to retain some memory of the FSD in sea ice models. The consolidation of the joints between floes is likely to take more time than the simple freezing of the sea surface or the welding of floes together during freezing conditions, which can occur in a few hours. The timescale associated with the consolidation is certainly more similar to the mechanical "healing" of sea ice in neXtSIM described in Rampal et al. (2016), with values of $\simeq$ 10-30 days.

We therefore implemented two variables in neXtSIM to represent the evolution of floes over these two different timescales. The first one, that we call the "thermodynamical" FSD $g_{\mathrm{thermo}}(D,\boldsymbol{x},t)$, corresponds to the FSD that what would be seen by a satellite image for example, and represents the evolution of floe size associated to thermodynamical growth or melt. The second one, that we call the "mechanical" FSD, $g_{\mathrm{mech}}(D,\boldsymbol{x},t)$, aims to represent the evolution of floes associated with fragmentation and mechanical "healing". To keep a memory of fragmentation events over longer timescales, the floe size growth in $g_{\mathrm{mech}}(D,\boldsymbol{x},t)$ occurs at a slower rate than in g_{thermo}. Note that here, D is the floe size defined as the caliper diameter of the floes following Rothrock and Thorndike (1984). These two FSDs are implemented in neXtSIM as areal FSDs similarly to Zhang et al. (2015), Roach et al. (2018), Bateson et al. (2019), Boutin et al. (2019) and others, and are defined as:

$$\int_{D}^{D+dD} g(D,\boldsymbol{x},t)dD = \frac{1}{A}a_D(D,D+dD), \tag{1}$$

and

$$\int_{0}^{\infty} g(D,\boldsymbol{x},t)dD = 1. \tag{2}$$

In these definitions, g represents an FSD, A is the total area considered around the position $\boldsymbol{x}$ at a time t, and a_D are the areas within A covered by sea ice with floes with diameters between D and $D+dD$ respectively. The value D=0 corresponds to open water, and Eq. 2 is equivalent to $\int_{0+}^{\infty} g(D,\boldsymbol{x},t)dD = c$, c being the sea ice concentration. In practice, we have a number N of FSD bins of constant width ΔD, with edges between a minimum and and a maximum floe size, respectively D_0 and

https://doi.org/10.5194/tc-2020-19
Preprint. Discussion started: 24 January 2020


The Cryosphere Discussions
Open Access
EGU

D_N. We take the category associated with the largest floes, associated with the floe size interval $[D_{N-1}D_N]$, as representing unbroken floes.

Both FSDs evolve as in Roach et al. (2018) or Boutin et al. (2019), following:

$$\frac{\partial g(D)}{\partial t} = -\nabla \cdot (\mathbf{u} g(D)) + \Phi_{\mathrm{th}} + \Phi_{\mathrm{m}}, \tag{3}$$

in which $\mathbf{u}$ corresponds to the sea ice velocity vector, Φ_{th} is a redistribution function of floe size due to thermodynamic processes (i.e. lateral growth/melt), and Φ_{m} is a mechanical redistribution function associated with processes like fragmentation, lead opening, ridging, and rafting. In our implementation, we assume that the only mechanical process modifying the shape of the FSD is the wave-induced sea ice fragmentation, and Φ_{m} is therefore the redistribution term associated to this process. The advection terms for both FSD are identical, and similar to what is done for other conservative sea ice properties in neXtSIM. The other terms, Φ_{th} and Φ_{m}, differ between g_{thermo} and g_{mech} and are described below.

2.2.1 Lateral sea ice melt/growth

In this section, we describe the implementation of the terms $\Phi_{\mathrm{th,mech}}$ and $\Phi_{\mathrm{th,thermo}}$ that represent the thermodynamical redistribution of floes associated with lateral melt/growth in each FSD. The evolution of the FSD due to ice growth and melt processes is first performed in the thermodynamical FSD, and is quite similar to the implementation described by Roach et al. (2018):

$$\Phi_{\mathrm{th,thermo}} = -2G_r \left(-\frac{\partial g_{\mathrm{thermo}}}{\partial D} + \frac{2}{D} g_{\mathrm{thermo}} \right) + \delta(D - D_N)\dot{c}_{\mathrm{new}} + \beta_{\mathrm{weld}} \tag{4}$$

where G_r is the lateral melt rate of floes, $\dot{c}_{\mathrm{new}}$ is the rate of formation of new ice, and β_{weld} is the FSD redistribution term associated with welding of floes, using the Smoluchowski equation as implemented by Roach et al. (2018).

Lateral melting is implemented following Horvat and Tziperman (2015) and Roach et al. (2018), with the additional assumption that floes in the largest floe category are not affected by lateral melt. We also do not make any distinction between what they call the "lead region" and the "open water fraction" of each grid cell, which means the factor called ϕ_{lead} in Roach et al. (2018) is taken to be 1. Note also that lateral melt will not be discussed here, as this study focuses on the impact of waves on sea ice dynamics during a time period dominated by freezing.

In contrast to Roach et al. (2018), sea ice is assumed to be unbroken when initialised in our model, and there is therefore no need for an explicit thermodynamical lateral growth due to the agglomeration of frazil ice at the edge of existing floes. If, after a wave-induced fragmentation event, the sea ice concentration reaches 1 in freezing conditions, it is assumed that the newly formed sea ice is filling all the leads, creating joints between the floes, and the thermodynamical FSD is therefore redistributed so that all ice is considered made of unbroken floes.

The growth of small floes resulting from wave-induced fragmentation in our model is also ensured by welding, which is shown by Roach et al. (2018) to generate a lateral growth rate one order of magnitude higher than that arising from the lateral accumulation of frazil ice. We, however, found the algorithm they use to be very dependent on the choice of the FSD categories. After some discussion with the authors of Roach et al. (2018), we decided to carry on with this formulation but with

https://doi.org/10.5194/tc-2020-19
Preprint. Discussion started: 24 January 2020


The Cryosphere Discussions

an appropriate tuning of the coefficient that Roach et al. (2018) call κ, which represents the rate at which the number of floes decreases due to welding per surface area. We tune κ so that the timescale at which a uniform FSD made of the smallest floes allowed in the model evolves into a uniform FSD made of the biggest possible floes is similar in our model and in the one by Roach et al. (2018). To give an idea of the time-scales involved, the model of Roach et al. (2018), starting from a uniform FSD only made of floes with an average size of 20 m, ends up with half of the ice cover being made of floes larger than 200 m in about 5 days within compact sea ice ($c = 0.95$). In the simulations presented in this study, setting $\kappa = 5 \times 10^{-8}$ reproduces a similar evolution of the FSD for our choice of FSD categories.

As mentioned earlier, the redistribution of the mechanical FSD due to lateral growth in $\Phi_{\mathrm{th,mech}}$ is expected to happen on longer timescales, related to the time needed by the fractures to heal. This healing phenomenon is related to the thickening and the consolidation of the joints of which formation is described in $\Phi_{\mathrm{th,thermo}}$. It is very similar to the "damage healing" already included in neXtSIM (see Rampal et al., 2016), associated with a timescale τ_{heal}, that we re-use in the computation of $\Phi_{\mathrm{th,mech}}$ following:

$$\Phi_{\mathrm{th,mech}} = \frac{1}{\tau_{\mathrm{heal}}} \big(g_{\mathrm{thermo}}(D) - g_{\mathrm{mech}}(D) \big). \tag{5}$$

As it is, the mechanical FSD therefore relaxes to the thermodynamical over a time τ_{heal}, representing the (slow) strengthening of the joints between the floes. Note that this healing only occurs if the sea ice is exposed to freezing conditions. In melting conditions, we assume that the shape of the mechanical FSD is not affected by lateral melt.

2.2.2 Wave-induced sea ice fragmentation

In this section, we describe the implementation of the terms $\Phi_{\mathrm{m,mech}}$ and $\Phi_{\mathrm{m,thermo}}$ that represent the mechanical redistribution of floes associated with the fragmentation of sea ice by waves in each FSD. As mentioned before, during a wave event, floes are likely to break at their weakest point, i.e the freshly refrozen joints between floes (Kohout et al., 2016). In the following, we assume that when waves are able to break sea ice, the old fractures in the ice cover are immediately re-activated. To represent this process, the mechanical redistribution is first performed in the mechanical FSD g_{mech}, in which the growth of the floe size is slower than in the thermodynamical FSD, and that has therefore kept a memory of previous fragmentation events. Besides, because sea ice fragmentation is a quick and violent phenomenon, it only needs a few minutes to impact the floe size. It is therefore likely to overcome all the thermodynamical processes going-on, as they are associated with longer timescales. When fragmentation occurs, we therefore revert the thermodynamical FSD g_{thermo} to g_{mech}. This is done by setting $\Phi_{\mathrm{m,thermo}} \Delta t = g_{\mathrm{thermo}} - g_{\mathrm{mech}}$, where Δt is the model time step.

Similarly to the work by Boutin et al. (2019), the occurrence of sea ice fragmentation in our coupled system is decided in the wave model. In WW3, sea ice breaks up if the wave curvature induces a stress that exceeds the sea ice flexural strength. The wave wavelength for which the wave-induced stress is maximum, that we call λ_{break}, is passed to neXtSIM (see Fig. 1) and used in the mechanical redistribution scheme of the FSD. The determination of the value of λ_{break} in WW3 is briefly

https://doi.org/10.5194/tc-2020-19
Preprint. Discussion started: 24 January 2020

summarized in appendix A. If no fragmentation has occurred in WW3, neXtSIM receives $\lambda_{\rm break} = 1000$ m, which corresponds to the default unbroken value, and no fragmentation occurs in neXtSIM (resulting in $\Phi_{\rm m,mech} = 0$ and $\Phi_{\rm m,thermo} = 0$).

If neXtSIM receives a value of $\lambda_{\rm break}$<1000 m, then FSD redistribution occurs in neXtSIM. The mechanical redistribution term can be written in the same form as in Zhang et al. (2015):

$$\Phi_{m,\rm mech} = -Q(D)g_{\rm mech}(D) + \int_0^\infty Q(D')\beta(D',D)g_{\rm mech}(D')dD' \tag{6}$$

where $Q(D)$ is a redistribution probability function characterising which proportion of floes of a given size D is going to be broken, and $\beta(D',D)$ is a redistribution factor quantifying the fraction of sea ice concentration transferred from one floe size to another as fragmentation occurs. The choice of $Q(D)$ and $\beta(D',D)$ will therefore shape the FSD resulting from wave-induced fragmentation. Here, we introduce new parameterizations for $Q(D)$ and $\beta(D',D)$ aiming to allow more freedom to the FSD evolution than in previous studies by Zhang et al. (2016) and Boutin et al. (2019).

In the absence of a wave model, Zhang et al. (2016) parameterize $Q(D)$ as a function of sea ice properties and wind speed. In their coupling, Boutin et al. (2019) pass the value of $\lambda_{\rm break}/2$ (which they call $D_{\rm max}$) from WW3 to the sea ice model and assume it corresponds to the new upper-limit of truncated power-law FSD with a fixed exponent, just like in the studies by Dumont et al. (2011) and Williams et al. (2013b). They arbitrarily set the values of $Q(D)$ and $\beta(D',D)$ to this purpose. Here, using the wave field information provided by WW3, but not constraining *a priori* the shape of the redistributed FSD, we define $Q(D)$ as:

$$Q(D) = \frac{1}{\tau_{WF}} p_{\rm FS}(D, D_{\rm FS}) p_\lambda(D, \lambda_{\rm break}), \tag{7}$$

in which $\tau_{\rm WF}$ is a relaxation time associated with wave-induced fragmentation events, used to remove dependency on the time step, and $p_{\rm FS}$ and p_λ are probabilities that floes break depending on their size. We set $\tau_{\rm WF}$ to 30 minutes, as it corresponds to the timescale of the fragmentation event described in Collins et al. (2015).

In the absence of known relationships linking wave and sea ice properties to floe break-up probabilities, we use $p_{\rm FS}$ and p_λ to express the idea that the smaller the floes are, the less chance they have to break. The function $p_{\rm FS}$ compares the floe size D with the minimum floe size for which flexural failure can occur, $D_{\rm FS}$ (see Mellor, 1986), which is computed as:

$$D_{\rm FS} = \frac{1}{2}\left(\frac{\pi^4 Y h^3}{48\rho g(1-\nu^2)}\right)^{1/4} \tag{8}$$

where g is gravity and ρ is the density of sea water. The value of $p_{\rm FS}$ therefore only depends on sea ice properties. Similarly, the function p_λ compares the floe size D with the wave wavelength associated with the highest stress experienced by sea ice

https://doi.org/10.5194/tc-2020-19
Preprint. Discussion started: 24 January 2020

λ_{break}, introducing a dependency of $Q(D)$ on the wave field. These two probabilities are heuristically defined as:

$$p_{\mathrm{FS}}(D) = \max\left(0, \tanh\left(\frac{D - c_{1,\mathrm{FS}} D_{\mathrm{FS}}}{c_{2,\mathrm{FS}} D_{\mathrm{FS}}}\right)\right), \tag{9a}$$

$$p_{\lambda}(D, \lambda_{\mathrm{break}}) = \max\left(0, \tanh\left(\frac{D - c_{1,\lambda} \lambda_{\mathrm{break}}}{c_{2,\lambda} \lambda_{\mathrm{break}}}\right)\right), \tag{9b}$$

in which $c_{1,\mathrm{FS}}$, $c_{2,\mathrm{FS}}$, $c_{1,\lambda}$, and $c_{2,\lambda}$ are tuning parameters. As floes smaller than D_{FS} cannot be broken, we set $c_{1,\mathrm{FS}} = 1$. To compute wave attenuation in WW3, Boutin et al. (2018) make the hypothesis that floes smaller than $0.3\lambda_{\mathrm{break}}$ are tilted by waves but do not bend. They have therefore no chance of suffering flexural failure. To stay coherent with this hypothesis, we set $c_{1,\lambda}$=0.3. The values of $c_{2,\mathrm{FS}}$ and $c_{2,\lambda}$ control the range over which p_{FS} and p_{λ} go from 0 to 1. We set $c_{2,\mathrm{FS}} = 2$ and $c_{2,\lambda} = 2$. Theses choices are discussed in section 4.1.2 and B.

Similarly to the work by Zhang et al. (2015) and Boutin et al. (2019), the redistribution factor β follows the form, for D' in $[D_n\ D_{n-1}]$:

$$\begin{cases} \beta(D, D') = \dfrac{D_n^q - D_{n-1}^q}{D_2^q - D_1^q} \text{ if } D_n \geq D \\ \beta(D, D') = 0 \text{ otherwise} \end{cases} \tag{10}$$

where n corresponds to the index of the n^{th} FSD category, D_2 and D_1 are the limits of the floe size range over within which broken floes are redistributed, and q is an exponent that will set the shape of the redistributed FSD. Zhang et al. (2015) use $q = 1$, arguing that the fragmentation of floes being a stochastic process, any floe size lower than the initial unbroken floe can be generated with a similar probability. It leads to power-law FSDs after a succession of fragmentation events. Their assumption, however, contradicts the experimental results of Herman et al. (2018) who observe a preferred floe size in the FSD resulting from the fragmentation of a thin sea ice cover in a tank. To keep coherent with the exponent $\gamma = 1.9$ of the truncated power-law assumed in the FSD parameterization implemented in WW3 following Williams et al. (2013b), Boutin et al. (2019) use $q = 2 - \gamma$. In our case, the wave model does not need any parameterization of the FSD to provide the maximum and average floe size: the FSD only exists in neXtSIM, and these parameters are now computed in the sea ice model from the FSD. We can therefore here give more freedom to the FSD evolution, and aim to reproduce FSDs similar to what observed in the field (e.g, as reported by Toyota et al., 2011) and laboratory (e.g Herman et al., 2018) experiments. We suggest here the following parameterization:

$$D_1 = D_0, \tag{11a}$$

$$D_2 = D, \tag{11b}$$

$$q = -\log_2(p_{\mathrm{FS}}(D) p_{\lambda}(D, \lambda_{\mathrm{break}})) \tag{11c}$$

The choices of D_1 and D_2 ensure sea ice conservation (see Zhang et al., 2015). The function used for q is very similar to the parameter called fragility in the studies by Toyota et al. (2011) and Dumont et al. (2011). The FSD redistribution generated

https://doi.org/10.5194/tc-2020-19
Preprint. Discussion started: 24 January 2020

by this parameterization allows us to generate FSDs resulting from wave-induced sea ice fragmentation that reproduce some of the features reported in observations, in particular: the existence of two regimes with a cut-off floe size and a power-law cumulative number of floes distribution with an exponent between 0 and 2 for the small floe regime. This is shown and briefly discussed in section 4.1.2.

The processes we use for the wave-in-ice attenuation computation in WW3 require the estimation of two floe size parameters: the average floe size $\langle D \rangle$ and the maximum floe size $D_{\max}$ (Boutin et al., 2018). When WW3 is ran as a stand-alone, $D_{\max}$ is taken to be $\lambda_{\text{break}}/2$ (see appendix A) and an assumption made on the shape of the FSD after fragmentation allows to estimate the value of $\langle D \rangle$. When WW3 is coupled with neXtSIM, the FSD is free to evolve to the sea ice model, and it is necessary to estimate the value of $D_{\max}$ and $\langle D \rangle$ in neXtSIM so it can be sent to WW3.

The average floe size $\langle D \rangle$ can be simply defined as

$$\langle D \rangle = \int_0^\infty g_{\text{mech}}(D) dD. \tag{12}$$

Here we use the mechanical FSD $g_{\text{mech}}(D)$ assuming that wave scattering, which is the wave attenuation process depending on $\langle D \rangle$, is more affected by consolidated floes than by the thin ice jointing them. The maximum floe size $D_{\max}$ definition is less straightforward, as it was originally designed in the FSD parameterization of Dumont et al. (2011) to represent the largest floe size of a fragmented sea ice cover, and if no fragmentation had occurred it was set to a large default value. Here, this definition needs to be extended to a coupled-system with an FSD free to evolve under the effects of both mechanical and thermodynamical processes, able to represent a mix of fragmented floes and large ice plates. We suggest a definition based on the percentage of the ice cover area occupied by large floes, computing $D_{\max}$ as the 90^{th} percentile of the areal FSD. Moreover, since $D_{\max}$ is used in WW3 as an indication of the elasticity of the floes experienced by the wave depending on their wavelength, we have to make sure that a fully unbroken sea ice cover has a value of $D_{\max}$ one order of magnitude higher than the longest wave wavelength used in WW3 (for instance 1000 m in Boutin et al., 2018). To do so, once the proportion of sea ice in the largest floe size category $\int_{D_{N-1}}^{D_N} g_{\text{mech}}(D) dD/c$ exceeds 10%, we make $D_{\max}$ grow linearly with $\int_{D_{N-1}}^{D_N} g_{\text{mech}}(D) dD/c$ from D_N to 1000 m when $\int_{D_{N-1}}^{D_N} g_{\text{mech}}(D) dD/c$=1.

2.3 Link between wave-induced sea ice fragmentation and damage

As mentioned in the introduction, it is expected that sea ice fragmentation by waves results in lowering the ice internal stress. The lowering of sea ice resistance to deformation due to the high density of cracks is already included in neXtSIM, with the variable called damage. This variable takes value between 0 and 1, with 0 corresponding to undamaged sea ice, and 1 to a highly damaged sea ice cover, i.e. presenting a high-density of cracks. Sea ice damaging in neXtSIM is usually due to the wind. In our study, we would like it to have an additional dependence on wave-induced sea ice fragmentation. In our implementation, it is possible to quantify the sea ice cover area that is susceptible to be broken by waves if WW3 provides a

https://doi.org/10.5194/tc-2020-19
Preprint. Discussion started: 24 January 2020

value of $\lambda_{\rm break} < 1000$ m as $c_{\rm broken} = c\left(1 - {\rm e}^{-\Delta t/\tau_{WF}}\right)$, and $c_{\rm broken} = 0$ if $\lambda_{\rm break} \geq 1000$ m. As the fragmentation of sea ice by waves can break ice plates into floes with sizes up to a few hundred metres, and as the horizontal resolution of the model mesh is in general of at least a few kilometres, we make the hypothesis that areas of the sea ice cover fragmented by waves are associated with high values of damage, i.e. close to 1. We thus suggest to compute the new damage value associating a value of d_w =0.99 to $c_{\rm broken}$, which gives the following evolution of the damage d:

$$d = \min\left(1, d(1 - c_{\rm broken}) + d_w c_{\rm broken}\right) \tag{13}$$

This process is repeated every time fragmentation occurs in the sea ice model. Note that, because wave events generally last for a few hours, this damaging process is generally repeated enough times to result in little sensitivity of the model to values of d_w between 0.1 and 1.

3 Model set-up

3.1 General description of the pan-Arctic Configuration

Similarly to Boutin et al. (2019), the coupled framework is run on a regional 0.25° grid (CREG025), which covers the Arctic Ocean at an approximate resolution of 12 km, as well as some of the North Atlantic. As neXtSIM is a finite elements sea ice model using a moving Lagrangian mesh, it is not run on a grid. Its initial mesh is, however, based on a triangulation of the CREG025 grid, giving a prescribed mean resolution (i.e. mean length of the edges of the triangular elements) of 12 km. In coupled mode, neXtSIM interpolates the fields to be exchanged onto the fixed grid, so that the coupler, OASIS, is only required to send and receive different fields (i.e. OASIS does not need to do any interpolation).

neXtSIM is run with a timestep of 20 s, and WW3 with a timestep of 800 s. Fields between the two models are exchanged every 2400 s. Atmospheric forcings are provided by 6-hourly fields from the CFSv2 atmospheric reanalysis (Saha et al., 2014). In addition, neXtSIM is also forced by ocean fields from the TOPAZ4 reanalysis (Sakov et al., 2012). For more details on the forcings used by neXtSIM, see Rampal et al. (2016). Wave-currents interactions in WW3 are not considered in this study.

For the FSD in neXtSIM, we use 20 categories with a width ΔD =10 m. The lower bound D_0 is set to 10 m, which is about the size of the smallest floes susceptible to undergo flexural failure (Mellor, 1986). The upper bound of the FSD, D_N, is therefore equal to 210 m, which is of the order of magnitude of the largest floes resulting from wave-induced sea ice fragmentation generated by WW3. The healing relaxation time $\tau_{\rm heal}$ used by neXtSIM is set to its default value of 25 days.

3.2 Evaluation of the FSD implementation: model set-up

In section 4.1, we make use of sea state and sea ice observations realised in the Beaufort Sea in the framework of the Arctic Sea State and Boundary Layer Physics Program (Thomson et al., 2018) to evaluate the wave attenuation and broken sea ice extent in our coupled simulations, similarly to what Ardhuin et al. (2018) did with stand-alone WW3 simulations. To do so, we

https://doi.org/10.5194/tc-2020-19
Preprint. Discussion started: 24 January 2020

run 5 simulations from October 10^{th}, 2015 to October 13^{th}, 2015, a period covering the storm event investigated in a study by Ardhuin et al. (2018). This storm is associated with $\simeq$4-m-waves fragmenting the sea ice edge in the Beaufort Sea from 11-12 October 2015.

The first of these simulations is a WW3 uncoupled simulation hereafter labelled ARD18 as it uses the exact same parameterization as the one labelled REF2 in Ardhuin et al. (2018). The only difference is that here it is run on the CREG025 grid used for all our simulations. This parameterization of the wave model is chosen as it is the one showing the best match with observations for both wave height and broken sea ice extent in the study by Ardhuin et al. (2018). We also use the same sea ice concentration data as Ardhuin et al. (2018) to force the uncoupled wave model. They are obtained from a reanalysis of the 3-km resolution sea ice concentration dataset derived from the AMRS2 radiometer using the ASI algorithm (Kaleschke et al., 2001; Spreen et al., 2008, available at https://seaice.uni-bremen.de/data/amsr2/asi_daygrid_swath/n3125/2015/oct/Arctic3125/, visited early 2018). This reanalysis produces 12-hourly maps that gather all the AMSR2 passes acquired between 00:00 and 13:59 UTC, and 10:00 and 23:59 UTC for the morning (AM) and evening (PM) fields, respectively. Similarly to Ardhuin et al. (2018), sea ice thickness is set constant to 15 cm. Sea ice concentration is also kept constant to make the comparison with a coupled simulation easier. Sea ice concentration for this 3-day run corresponds to the conditions of the evening of October 12^{th} provided by the AMSR-2 sea ice concentration reanalysis, at the same time as illustrated in Ardhuin et al. (2018) study. Initial wave conditions are provided by an initial 10-days run of this simulation, from October 1^{st} to October 10^{th}, 2015, in which sea ice concentration is updated every 12h.

Secondly, we run a coupled neXtSIM-WW3 simulation (hereafter labelled NXM/WW3). Initial conditions are the same as in ARD18. Sea ice dynamics and thermodynamics are switched off in neXtSIM, so that we can compare the two simulations with a similar constant sea ice cover (thickness and concentration), the only difference between ARD18 and NXM/WW3 being the way the evolution of floe size is treated, which is what we want to evaluate.

Then, to illustrate the sensitivity of our results to the sea ice thickness value, we re-run ARD18 and NXM/WW3 while setting this time the sea ice thickness to 30 cm. We name these two additional simulations ARD18_H30 and NXM/WW3_H30 respectively.

Finally, to investigate the sensitivity of the FSD evolution to the floe size categories used for the FSD, we run a a simulation similar to NXM/WW3 but with a refined FSD that we call NXM/WW3_refine. For this simulation, the number N of categories is set to 41 instead of 20, and we set ΔD=5 m and D_0 =5 m.

3.3 Estimation of the impact of wave-induced fragmentation on sea ice dynamics: model set-up

In section 4.2, we compare the results of 3 simulations in order to investigate the wave impact on sea ice dynamics in the MIZ. The first one (called REF) is a stand-alone simulation of neXtSIM. The second one (CPL_WRS) includes all the features

https://doi.org/10.5194/tc-2020-19
Preprint. Discussion started: 24 January 2020

presented in section 2 but the relationship between wave-induced sea ice fragmentation and damage presented in 2.3. The third (CPL_DMG) is similar to CPL_WRS except that it also includes a link between the damage variable d and wave-induced sea ice fragmentation as described in section 2.3. These simulations are ran for a period going from September 15$^{\text{th}}$ to November 1$^{\text{st}}$ 2015. This period was selected as refreezing occurs in the MIZ, meaning that the differences between REF and the two coupled simulations are not due to the change in lateral melting parameterization. It also includes storms, allowing to evaluate the behaviour of sea ice after large fragmentation events. The level of damage in the ice cover is initially set to zero where sea ice is present. Initial sea ice concentration and thickness are set from the TOPAZ4 reanalysis (Sakov et al., 2012), and sea ice is unbroken. The wave field in WW3 is initially at rest. The wave-in-ice attenuation parameterization in WW3 in CPL_WRS and CPL_DMG is the same as in ARD18 (i.e. REF2 in Ardhuin et al., 2018). We investigate the results of these simulations from October 1$^{\text{st}}$, thus allowing for 16 days of spin-up, which is enough for the wave and damage fields to develop.

4 Results

4.1 Evaluation of wave–sea-ice interactions in the coupled framework

We first evaluate the representation of wave-ice interactions in our coupled framework. As our goal is to investigate the potential impact of waves on sea ice dynamics, we must ensure that the coupled framework produces a consistent wave-in-ice attenuation, as it is directly proportional to the WRS, as well as reasonable extents of broken sea ice and timescales of the ice recovery from fragmentation. In the following, we will consider the wave attenuation and extent of fragmented sea ice on the one hand, and the evolution of the FSDs after fragmentation events on the other hand.

4.1.1 Evaluation of wave attenuation and extent of fragmented sea ice

To evaluate the capacity of our coupled framework to produce reasonable wave-in-ice attenuation and extent of broken sea ice, we focus on the same event used to evaluate the WW3 parameterization of Boutin et al. (2018) in the study by Ardhuin et al. (2018). Here, we use the ARD18 simulation as a reference, as it was shown to give very satisfactory results for both the extent of broken ice and the wave attenuation in this particular case. The comparison is done on October 12th, at 17:00 GMT (Fig. 2). We also compare our model results with estimated wave height from SAR images (Stopa et al., 2018a) and buoy measurements (AWAC, see Thomson et al., 2018) along a transect in Figure 2d.

The extent of broken ice is very similar in the two simulations, although slightly smaller in the coupled run (Fig. 2c). This difference does not, however, exceed 2 grid cells, therefore representing a distance of about 25 km, which is perfectly acceptable given the uncertainties associated with wave attenuation in ice. Moreover, as in Ardhuin et al. (2018), the broken sea ice region extends up to about 15 km in-ice beyond the AWAC buoy (red square), which matches well with the observation as on Synthetic Aperture Radar (SAR) images for that same day.

https://doi.org/10.5194/tc-2020-19
Preprint. Discussion started: 24 January 2020

We evaluate the wave attenuation by looking at the evolution of the maximum floe size $D_{\max}$ and significant wave height in the ice. The spatial distribution of these two quantities is overall very similar between ARD18 and NXM/WW3, and also very similar to the results of Ardhuin et al. (2018) (see Figure 9 of their study). Figure 2d shows the wave height evolution along a transect following the footprint of Sentinel 1-a, and again we see almost no difference between ARD18 and NXM/WW3. Both simulations show reasonable agreement with the wave heights estimated from SAR and from the AWAC buoy. Similarly to the results of Ardhuin et al. (2018), the model, however, seems to slightly overestimate the wave height within the ice cover. This overestimation could result from the assumption of constant thickness and its low value (15 cm). This is visible on Figure 2d where most observations actually show higher significant wave height values than the one yielded by ARD18_H30 and NXM/WW3_H30, that use a constant thickness of 30 cm.

4.1.2 Evaluation of the evolution of the FSDs

The other main novelties of our coupled framework are the simultaneous evolution of the two FSDs it includes, and the redistribution scheme used when wave-induced sea ice fragmentation occurs. We thus want to make sure that the shape of the FSD simulated by neXtSIM is consistant with the FSD observations available in the literature. As the simulations in this study focus on fall-period, when the sea ice cover expands due to freezing, we also check that the timescales associated with freezing and sea ice healing are reasonable. Note that because thermodynamical and dynamical processes are unactivated in NXM/WW3, the thermodynamical and mechanical FSDs are identical.

We first look at the FSD resulting from wave-induced fragmentation in neXtSIM by plotting the cumulative distribution of floes (CDF, see e.g. Herman et al., 2018) for 3 different locations (Fig. 3) for the NXM/WW3 and NXM/WW3_refine simulations. Similar to field and laboratory observations (see for instance Toyota et al., 2011; Herman et al., 2018), we can distinguish two regimes separated by a cut-off floe size: (i) a small floe regime, that follows a power-law, and (ii) a large floe regime, with a much steeper slope of the CDF. Just like in the observations by Toyota et al. (2011), the cut-off floe size and the (negative) power-law exponent of the small floe regime increase with the distance from the ice edge. For the two simulations, all but one value of the (negative) power-law exponents related to the small floe-regime are greater than -2, as expected for a CDF depending on a 2-D fragmentation process (Toyota et al., 2011). The one value of the exponent that does not lie in this range is obtained for the NXM/WW3 run close to the ice edge, where the cut-off floe size is too close to the value of D_0 for the small floe size regime to be resolved. Note also that the values of $D_{\max}$ for each location show little sensitivity to the FSD definition, with a maximum difference between the two simulations presented on 3 not exceeding the value of ΔD in the refined-FSD simulation (5 m). Considering the large uncertainties due to the little knowledge of wave-ice interactions, choosing $\Delta D = 10$ m instead of more refined FSDs in our coupled framework has therefore little impact on the wave attenuation computed in WW3.

Figures 4 and 5 illustrate the evolution of the FSDs in the CPL_DMG simulation, in which both mechanical and thermodynamical processes are active. Figures 4(a,c) show the proportion of "unbroken" ice (the proportion of sea ice associated with the N^{th} category of the FSD) for the thermodynamical and mechanical FSDs respectively, 17 days after the beginning of the

https://doi.org/10.5194/tc-2020-19
Preprint. Discussion started: 24 January 2020

simulation, leaving enough time for the waves and sea ice to spin-up. The regions of broken ice are relatively similar for both FSDs with the exception of the Barents Sea area. They actually closely follow the contour of 1-metre thick ice (not shown), after which the waves are too attenuated to fragment the sea ice. The Barents Sea area shows a wide area of broken thin ice in the mechanical FSD, with only parts of this region being broken in the thermodynamical FSD. This wide broken area is related to a strong wave event in this region occurring between 30/09/2015 and 01/10/2015. This event is associated with wave height up to 9 m and waves with period above 12 s propagating far into an ice cover made of relatively thin ice. About 24 hours after the event (not shown), the thermodynamical FSD in pack ice has mostly "recovered" due to welding and freezing in leads. In compact ice, this quick re-generation of large floe size has been eased by the large λ values associated with the long waves, making welding very efficient. This can be seen on Figure 4e, in which $D_{\max}$ exhibits large values far from the ice edge. The re-generation of large floes in the mechanical FSD takes much longer, with a timescale set by the value of τ_{heal} (25 days in CPL_DMG), and the end of the mechanical healing of the Barents Sea area is still visible on 01/11/2015 (Fig. 4d).

This difference in timescales is also visible in Figure 5, which illustrates the evolution of the thermodynamical and mechanical FSDs (a,c) and CDFs (b,c) for the location indicated by a cross on Figure 4(a,c), at the time of shown on the snapshot (02/10/2015 at 00:00:00 GMT) and 24 hours later. On 02/10/2015 the proportion of sea ice that is unbroken is almost 0 in the mechanical FSD, while welding and refreezing in thermodynamical FSD have allowed the re-formation of unbroken sea ice over more than 10% of the ice-covered part of the mesh element. The action of welding and refreezing in the thermodynamical FSD results in a steepening of the slope of the CDF associated with the small floe regime, and flatten the slope of the large floes regime. The mechanical FSD shows no sign of any healing, the last fragmentation event being too recent, and its associated CDF clearly show a small and a large floes regime resulting from the fragmentation by waves (Fig. 4). 24 hours later, more than 95% of the thermodynamical FSD consists of unbroken sea ice, while the mechanical FSD is still very similar to what it was on the previous day, illustrating the memory effect of the mechanical FSD.

In summary, once the wave activity has decreased, refreezing and welding allow for a re-generation of a completely unbroken sea ice cover in timescales of a few hours to a few days in the thermodynamical FSD, depending on the initial level of fragmentation. The timescale over which the mechanical FSD re-generates large floes is associated with the value of τ_{heal}. As an indication of time, in the case illustrated here, with freezing conditions and compact ice, it takes about 4 days for the value of $D_{\max}$ to grow over 200 m.

4.2 Impact of sea ice fragmentation on sea ice dynamics in the MIZ

4.2.1 Case study: a fragmentation event in the Barents Sea (15-25 Oct. 2015)

To better understand the impact of (i) the WRS and (ii) fragmentation-induced damage on sea ice dynamics, we compare the results given by the REF, CPL_WRS, and CPL_DMG simulations in the Barents sea. Focusing only on this region simplifies the analysis, as this area is exposed to wave and sea ice conditions that experience little variations over the investigated period.

https://doi.org/10.5194/tc-2020-19
Preprint. Discussion started: 24 January 2020

It is particularly true for the fetch that allows intense wave events all along the simulations. It is also the case for the sea ice edge that remains oriented mostly east-west. In our analysis, we can therefore consider southward winds to be mostly off-ice, and conversely that northward winds to be directed on-ice. The domain we define to perform our analysis is limited south and north by the 69° and 84° parallels respectively, and west and east by the 16° and 60° meridians (see for instance Fig. 6).

To highlight the various responses of sea ice to fragmentation depending on wind and waves conditions, we select a particular fragmentation event occurring on October 15$^{\mathrm{th}}$ 2015 (see Fig. 6 for the initial sea ice conditions) which results in a growth of the surface occupied by broken ice (Fig. 7c). The 10 days following this event include both on-ice and off-ice conditions, allowing us to explore the impact of wave-induced sea ice fragmentation on sea ice dynamics in both cases.

The fragmentation event occurs during on-ice wind conditions (see the positive meridional component in Fig. 7a), with high waves (up to 5m at the ice edge) propagating far into the ice cover (see Fig. 7b and Fig. 8b). It results in an increase of the surface area made of recently broken sea ice in the domain (see for instance the evolution of the magenta contour between Fig. 6a and Fig. 8a), until it represents nearly 60% of the sea ice-covered part of the domain (Fig. 7c). Here we define the sea ice covered part of the domain as the area for which sea ice concentration $c > 0$. Recently-broken ice is defined as the region for which $D_{\max} \leq 200\,\mathrm{m}$, thus corresponding to fragmented sea ice for which refreezing has not yet had time to regenerate a significant proportion of unbroken ice (at least 10%). In the domain, the recently-broken sea ice area is mostly made of compact sea ice (that we define as the area of the domain for which $c > 0.8$). At the end of the fragmentation event, 80% of the recently-broken sea ice is made of compact ice, and it represents nearly 40% of the ice-covered part of domain (Fig. 7c). Compact sea ice being broken is important in the scope of our study, as low-concentration sea ice experiences little resistance to deformation due to its low effective stiffness, and is therefore largely unaffected by damage.

In the days following the fragmentation event, wind speed decreases and changes direction to become mostly southward (Fig. 7a). The wind speed then increases again, with a second maximum on October 20$^{\mathrm{th}}$, corresponding this time to off-ice winds. The generated waves tend to propagate away from the sea ice, resulting in low wave heights inside the ice (Fig. 7b). It coincides with a decrease in recently-broken sea ice surface area, which stops when the wind turns again to become parallel to the sea ice edge (Fig. 7c). This decrease is mostly due to sea ice recovering in the absence of waves, and can be seen by comparing the distributions of sea ice thickness and damage on October 16$^{\mathrm{th}}$ (Fig. 8a and 9a) and October 21$^{\mathrm{st}}$ (Fig. 8c and 9c), in which the limit between broken and unbroken ice tends to get closer to the ice edge, while damage in pack ice has visibly decreased. The band of recently broken ice remains however much larger than it was initially (Fig. 6b), as fragmented sea ice produce lower wave attenuation, thus allowing for sea ice fragmentation even in low wave height conditions.

https://doi.org/10.5194/tc-2020-19
Preprint. Discussion started: 24 January 2020

4.2.2 Effects of linking damage and sea ice fragmentation on sea ice dynamics in the MIZ

The conditions of the studied period now being described, the impact of adding the WRS and a relationship between wave-induced fragmentation and damage can be investigated. We first proceed by comparing (in Figure 10) the ice drift velocity averaged over the ice-covered domain for the 3 simulations: REF, CPL_WRS and CPL_DMG. Overall, we observe no differences in the trends, however, the magnitudes of the ice drift velocities show intermittent differences between these 3 simulations. These differences have two maxima, the first one on October 16 at 18:00:00 GMT, and the second one on October 21 at 09:00:00 GMT. To understand these differences, we compare the CPL_DMG and REF simulations at these two dates.

On October 16^{th}, wind and waves are directed on-ice, thus compacting the sea ice (Fig. 8b). At the time of the snapshot, sea ice has been recently broken over a wide surface area (within the magenta contour in Figures 8(a,b),9(a,b) and 11(a,b). It results in the damage value being maximum everywhere in this recently broken sea ice area in the CPL_DMG simulation (Fig. 9a). Comparing damage between the CPL_DMG and REF simulations (Fig. 9b), we note that the increase in damage related to wave-induced fragmentation is responsible is strong at the immediate proximity of the ice edge, and lower but still sensible ($\simeq 0.05$) closer to the limit between broken and unbroken ice. Comparing Figure 9b with Figure 11b, it is interesting to note that the highest difference in the magnitude of ice drift velocities between CPL_DMG and REF is mostly located in this area where the increase in damage due to wave is limited (Fig. 11b). This result is at first counter-intuitive, the biggest impact on the sea ice drift occurring where the impact on damage is the weakest, but it is due to the nature of sea ice at the limit between broken and unbroken ice, which is thicker and more compact than at the proximity of the ice edge. As mentioned before, thin, loose sea ice does not provide much resistance to deformation. For such sea ice, the level of damage has therefore little impact on its behaviour. Oppositely, thick compact ice is associated with high ice strength values, and its level of damage significantly impacts its resistance to deformation. The additional damage of thick compact ice due to wave-induced fragmentation, despite being small, allows for more sea ice convergence than in the REF and CPL_DMG simulations. Similarly, on October 21^{st}, the difference in ice drift velocity between CPL_DMG and REF is mostly due to an acceleration of compact sea ice that has been recently broken (Figure 11d). This acceleration follows the wind direction, creating additional convergence north of Svalbard, and divergence at the centre of the domain, thus increasing the export of sea ice this time.

To better quantify the impact of this additional damage on the dynamics of compact sea ice, we compare the ice drift velocity between the CPL_DMG and CPL_WRS simulations averaged over the area covered by compact and recently broken sea ice only in Figure 10b. This area includes all the ice within the domain delimited by the magenta and the green solid lines in Fig. 11(b,d). For this particular part of the sea ice cover, the differences in ice drift velocity magnitude are very significant, with an increase by more than 20% on October 16^{th}, and exceeding 40% on October 21^{st}. Over the whole 10 days following the fragmentation event, the ice drift velocity for recently broken and compact sea ice increases in average by 7% in CPL_DMG compared to CPL_WRS.

https://doi.org/10.5194/tc-2020-19
Preprint. Discussion started: 24 January 2020

We also note that for both events, the maximum in the ice drift velocity difference between CPL_DMG and the two other simulations (Fig. 10a,b) does not happen when the wind speed, ice drift velocity and wave height reach their maximum, but rather a few hours or days after they do (Fig.7a,b and Fig.10a). A possible explanation is that for strong winds and waves, the magnitude of the sum of the external stresses applied to the ice is high enough to overcome the ice internal stress (in all three simulations). However, for lower wind speeds and wave heights, the external stress magnitude decreases. In these conditions, only sea ice with a high enough damage value can still be deformed. The effect of additional damage is therefore more likely to be maximum in the wake of a storm than during the storm itself.

Waves also impact the sea ice dynamics through the WRS. Figures 8(b,d) show the relative importance of the WRS compared to the wind stress, as well as the direction in which both apply. On October 21 (Fig. 8d), the WRS exceeds the wind stress over the first kilometres of the sea ice cover, where the sea ice is rather thin and not compact. As described in Boutin et al. (2019), the WRS direction tends to be aligned with the wind at the sea ice edge, but further into the ice cover it aligns with the gradient of ice concentration or thickness. This is because the mean wave direction in the ice cover corresponds to the least attenuated waves, which tends to be the waves that have travelled the shortest distance in-ice. As a consequence, the WRS is most often directed on-ice, and thus a source of sea ice convergence (Stopa et al., 2018b; Sutherland and Dumont, 2018). When the WRS is taken into account, the external stress applied on sea ice during on-ice (respectively off-ice) wind conditions is enhanced (respectively reduced).

With our coupled-model, the impact of the WRS on the sea ice dynamics in the MIZ strongly depends on the activation of the link between wave-induced sea ice fragmentation and damage. In particular, these interactions between the WRS and sea ice damage contribute to some of the differences in ice drift velocity between the simulations we see on Figure 10a. For the October 21st case, we see a larger difference between CPL_DMG and CPL_WRS than between CPL_DMG and REF. In REF, the off-ice wind stress reduces the sea ice concentration, lowering its effective stiffness, so that sea ice drifts freely with the wind. In CPL_WRS, the WRS cancels some of the wind stress, as well as compacting the sea ice, which allows it to resist the off-ice external stress more. In CPL_DMG, the previous damage to the ice from the waves lowers its stiffness and it again drifts freely in the off-ice direction. The WRS thus limits the rate of sea ice export in off-ice wind events, to an extent determined by the rheology of the broken ice. Conversely, on October 16th (Fig. 8b), the wind stress is directed on-ice and therefore aligned with the WRS. Moreover, the relative importance of the WRS exceeds the one of the wind stress over a wide part of the recently broken sea ice area. In these conditions, the WRS contributes to accelerate the convergence of sea ice, which results in a larger difference of average ice drift velocity over the domain between CPL_DMG and REF than between CPL_DMG and CPL_WRS (Fig. 10a).

These interactions between sea ice damaging related to wave-induced fragmentation and WRS also have an impact on sea ice properties in the MIZ. Figure 12(a,b) displays the differences in the sea ice thickness and concentration fields between CPL_DMG and REF. tion of sea ice in the MIZ is clearly visible, with thicker, more compact sea ice in the area between

https://doi.org/10.5194/tc-2020-19
Preprint. Discussion started: 24 January 2020

the magenta and green solid lines, which corresponds to compact sea ice that has recently been broken. In contrast, between CPL_WRS and REF there are almost no differences in the sea ice thickness fields (Fig. 12c). Sea ice concentration is only impacted over the first kilometres of the ice cover, with compaction of the sea ice visible on the western part of the domain (*i.e.* lower sea ice concentration than in REF at the ice edge, but higher concentration slightly further in the ice cover, Fig. 12d). From this, we can conclude that when sea ice is damaged by wave-induced fragmentation, it enables sea ice convergence over all the broken sea ice area. As a consequence, on-ice wind events lead to thicker, more compact sea ice in the MIZ, and this phenomenon is enhanced by the WRS. When wave-induced sea ice fragmentation has no impact on sea ice rheology, compacted sea ice, if it is not damaged, resists convergence, preventing sea ice from thickening in the MIZ in CPL_WRS.

Note finally that the relative thickening of sea ice in CPL_DMG has a positive feedback on wave attenuation, leading to lower broken sea ice extent in CPL_DMG compared to CPL_WRS (visible on Fig. 12(b,d) for instance). As an example, in the domain we defined in the Barents sea, over all October, sea ice thickness is on average 2.9% thicker in CPL_DMG than in CPL_WRS, while the ratio of recently broken sea ice surface area over the total sea ice surface area decreases by 2.4% between CPL_DMG and CPL_WRS.

5 Discussion

In the previous section, we have shown with a case study that the damage added by wave-induced sea ice fragmentation does not significantly enhance sea ice deformation during extreme wind events, during which external stresses are already high enough to deform the ice. Instead, it creates a highly-damaged area vulnerable to further deformation, including in low-stress conditions. This behaviour of the MIZ, with fragmentation events followed by calm periods during which sea ice mobility is enhanced, is not limited to the particular event we describe here. In the Barents Sea, for instance, maxima in the difference between ice drift velocities in the CPL_WRS and CPL_DMG simulations during October 2015 occur after maxima in the ice drift velocity magnitude (Fig. 13), and we noted a similar behaviour in the Greenland Sea (not shown).

The impact of waves on sea ice dynamics is expected to vary spatially and temporally with waves and sea ice conditions in the Arctic. From our results, the magnitude of this impact depends mostly on the distance over which waves break the ice. At the beginning of October, the low sea ice extent combined with a high frequency of storms favours the occurrence of large fragmentation events, and waves therefore have a strong impact on sea ice dynamics in the MIZ. This impact seems to decrease towards the end of October, as visible on Figure 13 where the difference in drift speed between CPL_DMG and CPL_WRS does not show any more peaks after the one on October 21st. It coincides with refreezing in the Barents Sea: the generation of thin, sea ice over wide areas reduces the fetch and damps the waves over long distances, before they can break more compact sea ice. It is therefore likely that, in fall and winter, fragmentation will have little effect on sea ice dynamics as waves will be attenuated by the thin and loose forming sea ice. In contrast, in spring and summer, with the sea ice melt increasing the available fetch and exposing compact ice to the waves, we expect wave-induced sea ice fragmentation to have a significant impact on the MIZ. Note also that in melting conditions, sea ice healing will not occur, lengthening the effects of fragmentation over time.

https://doi.org/10.5194/tc-2020-19
Preprint. Discussion started: 24 January 2020

In addition to the effects of interactions between sea ice fragmentation and the WRS on sea ice dynamics, our study allows us to isolate the effect of the WRS in neXtSIM. The effects of the WRS in a coupled wave–sea-ice model system have already been discussed by Boutin et al. (2019) (coupling WW3 with the sea ice model LIM3) and Williams et al. (2017) (coupling neXtSIM and a simplified waves-in-ice model), and we will therefore only comment here on the main differences and similarities with these two studies. When the effect of wave-induced sea ice fragmentation on the dynamics is not included in the ice model (in CPL_WRS), the WRS pushes the sea ice edge towards pack ice and increases the sea ice concentration gradient over the first kilometres of the MIZ. This compaction is, however, limited to regions where sea ice opposes little resistance to deformation, either because it has a low concentration (hence ice strength) or because it has been previously damaged by the wind. It is similar to the results of the study by Boutin et al. (2019), in which they note that sea ice drift is only impacted by the WRS in low-concentration sea ice areas. However, Boutin et al. (2019) also found an acceleration by nearly 10% of the sea ice drift velocity in areas where sea ice has been broken compared to an uncoupled reference simulation. This is not the case in our study. The acceleration observed by Boutin et al. (2019) is attributed to the effect of the WRS on sea ice drift in regions with low sea ice concentration where waves can be generated in ice. In our simulations, low-concentration regions allowing for in-ice wave generation are very limited, and this effect is therefore not present. These differences in the sea ice concentration distributions might be related to the differences in the sea ice models and external forcings, but also to the different time period investigated. It is also interesting to note that Boutin et al. (2019) report a decrease of the sea ice melt in their coupled ocean-sea ice-wave framework, explained by the on-ice drift force associated with the WRS pushing sea ice away from the open water. In our case, we have described how sea ice that has been damaged by wave-induced fragmentation can be exported by an off-ice wind despite a resultant stress reduced by the on-ice push of the WRS. It would therefore be interesting to add an ocean component to our wave–sea-ice coupled framework, in order to compare the effects of wave–sea-ice interactions on sea surface properties with the results found by Boutin et al. (2019).

In the study by Williams et al. (2017), the WRS was shown to have little effect on the ice edge location, even when sea ice fragmentation was lowering the sea ice internal stress. The difference with our study is that we have assumed that fragmented sea ice is almost in free drift, while the EB rheology used by Williams et al. (2017) includes a *ad hoc* sea ice pressure term that gave some resistance to compression, which was especially needed once the ice became damaged (Rampal et al., 2016). The MEB rheology we use has been shown to give a better representation of sea ice deformation at pan-Arctic scale (Rampal et al., 2019) than EB, but this evaluation did not draw a particular attention to the MIZ. Assuming that fragmented sea ice is in free drift involves in particular neglecting the internal stress generated by the collisions and subsequent transfer of momentum between the floes (Shen et al., 1986). This additional stress is expected to reduce the sea ice convergence, lowering the thickening at the ice edge we report here. The acceleration of broken, compact sea ice we give here is therefore likely to be an upper bound of the effect of wave fragmentation on sea ice deformation.

An essential result of our model is the fact that after a storm, the region of sea ice susceptible to strong deformation extends considerably. One of the main uncertainties of our results therefore lies in the estimation of the area over which waves can break the ice. In our model, it depends mostly on two factors: the relaxation time associated with healing of damage (τ_{heal}), and the wave attenuation parameterization. The sensitivity to τ_{heal} was investigated by re-running our experiments using this

https://doi.org/10.5194/tc-2020-19
Preprint. Discussion started: 24 January 2020

time τ_{heal}=15 days, and found very little effect on our results. The sensitivity is possibly so low because once sea ice is broken, waves are able to propagate more easily in the sea ice cover and maintain quite a high level of damage until the wave activity strongly decreases, or until the sea ice cover extends. The extent of broken ice, however, depends strongly on the wave attenuation computed in WW3 (see Boutin et al., 2018). We have extended here the parameterization evaluated by Ardhuin et al. (2018) to a pan-Arctic simulation which can include very different sea ice conditions. This parameterization, like most wave-in-ice attenuation models, is very sensitive to the values of sea ice concentration and thickness (Doble and Bidlot, 2013), and the extent of broken sea ice we show here is therefore subject to very large uncertainties. Note, however, that the parameterization we selected is the one leading to the lowest sea ice extent in the study by Ardhuin et al. (2018). Moreover, the combination of wave attenuation processes we use (friction, inelastic dissipation and scattering) were shown by Boutin et al. (2018) to produce much stronger wave attenuation, and hence much lower broken sea ice extents, than scattering-only parameterizations (e.g Kohout and Meylan, 2008) from which are derived the attenuation coefficients used in the other studies investigating the effects of waves in sea ice models (Roach et al., 2018; Bennetts et al., 2017, for instance).

Although our main results are related to the effects of waves on sea ice dynamics, and only depend on the FSD's capacity to provide a good estimate for the maximum and average floe size used in the wave model, this work also takes the opportunity to introduce a coupled wave–sea-ice framework using two FSDs to represent both the mechanical and thermodynamical evolution of the floe size. The processes included theoretically allow us to represent the evolution of the FSD all-year round, even though simulations over different and longer time periods require further evaluation. The introduction of these two FSDs highlights the importance of distinguishing the different timescales involved in the floe size evolution.

As in the studies by Zhang et al. (2015) and Boutin et al. (2019), the main uncertainty related to the FSDs concerns the way sea ice is redistributed after fragmentation. The redistribution scheme we suggest here is quite flexible, generating CDFs very similar to what has been reported from both fields and laboratory experiments (Toyota et al., 2011; Herman et al., 2018). Its main characteristic is certainly its cut-off floe size that depends both on sea ice properties and on the wave field. This redistribution scheme could easily be adapted in case progress were made on the relative importance of the parameters affecting this cut-off floe size and the associated redistribution, either from observations thanks to new available FSD datasets (Hwang et al., 2017; Horvat et al., 2019), or from discrete element modelling (Herman, 2018). Note also that alternatives exist to the redistribution scheme of Zhang et al. (2015), and in particular the one suggested by Horvat and Tziperman (2015) that makes use of the whole wave frequency spectrum.

6 Conclusions

Using a coupled wave–sea-ice model, we have shown how waves may contribute to modifying the sea ice dynamics in the MIZ by lowering the resistance of compact sea ice to deformation. With our model, we note a significant acceleration of compact sea ice in both convergent and divergent sea ice drift conditions once sea ice has been fragmented by waves. Even though some assumptions we make here require further evaluation, the results are of particular interest as they highlight missing physics in current modelling systems used for short and long-term sea ice predictions, and concern key areas of the polar regions.

https://doi.org/10.5194/tc-2020-19
Preprint. Discussion started: 24 January 2020

Reliable sea ice forecasts are essential to ensure the safety of human activities close to the MIZ. In this context, waves pose a hazard as they make sea ice thicker and more mobile, and so our results stress the need for the addition of wave effects in sea ice models used in forecasts. On longer timescales, the impact of waves on sea ice dynamics could affect the amount of sea ice that is exported to the ocean. Indeed, eddies and/or filaments are likely to play an important role in this export in cases where sea ice dispersion is possible (Manucharyan and Thompson, 2017). Moreover, the fragmentation of sea ice itself could also generate sub-mesoscale (Horvat et al., 2016) and mesoscale activity in the ocean (Dai et al., 2019). Future coupling with an ocean model could therefore bring new insight into the interactions between waves, sea ice, and the ocean in the MIZ.

Code and data availability. Will be made available before final submission

Appendix A: Determination of $\lambda_{\mathbf{break}}$ in WW3

This section briefly summarises the way sea ice fragmentation is determined in WW3—more details and the values of all the parameters used in the break-up determination can be found in Boutin et al. (2018). In WW3, the value of the wave curvature is computed as:

$$\partial_x^2 \xi_{\mathrm{break}} = \sqrt{\max_{\forall k_i} \left(\frac{C_g}{G C_{g,i}} \int_{0.7k_i}^{1.3k_i} k_i^4 \omega N(k) \mathrm{d}k_i \right)} \tag{A1}$$

where C_g is the group velocity of waves in open water, $C_{g,i}$ is the group velocity of waves in ice, N is the wave action, ω is the wave pulsation and k_i is the wave wavenumber in ice. The associated significant stress that can cause the flexural failure of sea ice is then computed as:

$$\langle \sigma_{\mathrm{break}}^2 \rangle = \left(\frac{Yh}{2(1-\nu^2)} \partial_x^2 \xi_{\mathrm{break}} \right)^2, \tag{A2}$$

where Y is the Young's modulus, h is the ice thickness and ν is Poisson's ratio. Fragmentation occurs if this stress exceeds the flexural strength σ_{flex}, such as:

$$F_{\mathrm{break}} \sqrt{\langle \sigma_{\mathrm{break}}^2 \rangle} > \sigma_{\mathrm{flex}} \tag{A3}$$

F_{break} being the ratio of the maximum value of the strain to its root mean square value. In general, this ratio is a weakly increasing function of the duration considered. Similarly to Boutin et al. (2018), we set $F_{\mathrm{break}} = 3.6$ by considering the expected maximum amplitude in the succession of $N \simeq 500$ waves with Rayleigh-distributed amplitudes, during the time over which the sea state is approximately constant. The wavenumber $k_{i,\max}$ that produces the maximum stress above is then used to compute the wavelength $\lambda_{\mathrm{break}} = 2\pi / k_{i,\max}$. In a stand-alone run, WW3 relates this wavelength to the maximum floe size by setting $D_{\max} = \lambda_{\mathrm{break}}/2$. If Eq. A3 is not verified for any wavenumber k_i of the spectral wave model, λ_{break} is set to 1000 m, its default unbroken value.

https://doi.org/10.5194/tc-2020-19
Preprint. Discussion started: 24 January 2020


The Cryosphere Discussions
Open Access
EGU

Appendix B: Sensitivity of the FSD to the parameters used in the mechanical redistribution

The shape of the CDFs shown in Figures 3 and 5 strongly depend on the parameterization detailed in section 2.2.2. The value of the cut-off floe size at which the transition between the small and large floes regimes happens depends on the values of $c_{1,\lambda}\lambda_{\mathrm{break}}$ and $c_{1,\mathrm{FSD}}D_{\mathrm{FS}}$. Basically, if $c_{1,\lambda}\lambda_{\mathrm{break}} > c_{1,\mathrm{FSD}}D_{\mathrm{FS}}$, then the transition between the two regimes occurs around $c_{1,\lambda}\lambda_{\mathrm{break}}$. It thus depends mostly on the dominant wavelength of the waves (which is, however, strongly affected by the presence of sea ice). This is likely to happen close to the sea ice edge, where short waves are still able to penetrate. It is also the case in Figure 3, where sea ice is relatively thin, leading to a low value of D_{FS}. This behaviour of the CDF is coherent with the FSD parameterization suggested for wave models by Dumont et al. (2011), in which the maximum floe size depends on λ_{break}. Oppositely, if $c_{1,\lambda}\lambda_{\mathrm{break}} > c_{1,\mathrm{FSD}}D_{\mathrm{FS}}$, then the transition depends only on sea ice properties: elasticity and thickness. In their observations, Toyota et al. (2011) note that the cut-off floe size and the estimated value of D_{FS} are relatively close. This is also coherent with the results from the discrete elements model used by Herman et al. (2018), who found that the maximum stress location in floes flexed by waves showed little sensitivity to the wave spectrum. The coefficients $c_{2,\mathrm{FS}}$ and $c_{2,\lambda}$ can then be used to set the value of the slope of the two regimes. For instance, setting these coefficients to 1 leads to power-law exponents for the small floes regime very close to 2, with less variability between the ice edge and the limit of the broken extent (not shown).

Competing interests. The authors declare no competing interests.

Acknowledgements. This work has been carried out as part of the Copernicus Marine Environment Monitoring Service (CMEMS) WIzARd project. CMEMS is implemented by Mercator Ocean in the framework of a delegation agreement with the European Union. It has also been funded by institutional support from the Nansen Center. We finally thank Fabrice Ardhuin for providing us the data he used in a former publication and in particular the estimated wave height from SAR.

https://doi.org/10.5194/tc-2020-19
Preprint. Discussion started: 24 January 2020

References

Ardhuin, F., Sutherland, P., Doble, M., and Wadhams, P.: Ocean waves across the Arctic: Attenuation due to dissipation dominates over scattering for periods longer than 19s., Geophys. Res. Lett., 43, 5775–5783, https://doi.org/10.1002/2016GL068204, 2016.

Ardhuin, F., Boutin, G., Stopa, J., Girard-Ardhuin, F., Melsheimer, C., Thomson, J., Kohout, A., Doble, M., and Wadhams, P.: Wave attenuation through an Arctic marginal ice zone on 12 October 2015: 2. Numerical modeling of waves and associated ice breakup, Journal of Geophysical Research: Oceans, 123, 5652–5668, 2018.

Asplin, M. G., Galley, R., Barber, D. G., and Prinsenberg, S. J.: Fracture of summer perennial sea ice by ocean swell as a result of Arctic storms, J. Geophys. Res., 117, https://doi.org/10.1029/2011JC007221, 2012.

Azzara, A. J., Wang, H., Rutherford, D., Hurley, B. J., and Stephenson, S. R.: A 10-year projection of maritime activity in the US Arctic region, Tech. rep., 2015.

Bateson, A. W., Feltham, D. L., Schröder, D., Hosekova, L., Ridley, J. K., and Aksenov, Y.: Impact of floe size distribution on seasonal fragmentation and melt of Arctic sea ice, The Cryosphere Discussions, 2019, 1–35, https://doi.org/10.5194/tc-2019-44, https://www.the-cryosphere-discuss.net/tc-2019-44/, 2019.

Bennetts, L., O'Farrell, S., and Uotila, P.: Brief communication: Impacts of ocean-wave-induced breakup of Antarctic sea ice via thermodynamics in a stand-alone version of the CICE sea-ice model, The Cryosphere, 11, 1035–1040, https://doi.org/10.5194/tc-11-1035-2017, 2017.

Boutin, G., Ardhuin, F., Dumont, D., Sévigny, C., Girard-Ardhuin, F., and Accensi, M.: Floe Size Effect on Wave-Ice Interactions: Possible Effects, Implementation in Wave Model, and Evaluation, Journal of Geophysical Research: Oceans, 123, 4779–4805, https://doi.org/10.1029/2017JC013622, 2018.

Boutin, G., Lique, C., Ardhuin, F., Rousset, C., Talandier, C., Accensi, M., and Girard-Ardhuin, F.: Toward a coupled model to investigate wave-sea ice interactions in the Arctic marginal ice zone, The Cryosphere Discussions, 2019, 1–39, https://doi.org/10.5194/tc-2019-92, https://www.the-cryosphere-discuss.net/tc-2019-92/, 2019.

Cheng, S., Rogers, W. E., Thomson, J., Smith, M., Doble, M. J., Wadhams, P., Kohout, A. L., Lund, B., Persson, O. P., Collins, C. O., et al.: Calibrating a viscoelastic sea ice model for wave propagation in the arctic fall marginal ice zone, Journal of Geophysical Research: Oceans, 122, 8770–8793, 2017.

Collins, III, C. O., Rogers, W. E., Marchenko, A. V., and Babanin, A. V.: In Situ Measurements of an energetic wave event in the Arctic marginal ice zone, Geophys. Res. Lett., https://doi.org/10.1002/2015GL063063, 2015.

Craig, A., Valcke, S., and Coquart, L.: Development and performance of a new version of the OASIS coupler, OASIS3-MCT_3. 0, Geoscientific Model Development, 10, 3297, 2017.

Dai, H.-J., McWilliams, J. C., and Liang, J.-H.: Wave-driven mesoscale currents in a marginal ice zone, Ocean Modelling, 134, 1 – 17, https://doi.org/https://doi.org/10.1016/j.ocemod.2018.11.006, http://www.sciencedirect.com/science/article/pii/S1463500318303810, 2019.

Dansereau, V., Weiss, J., Saramito, P., and Lattes, P.: A Maxwell elasto-brittle rheology for sea ice modelling, The Cryosphere, 10, 1339–1359, 2016.

Doble, M. J. and Bidlot, J.-R.: Wave buoy measurements at the Antarctic sea ice edge compared with an enhanced ECMWF WAM: Progress towards global waves-in-ice modelling, Ocean Modelling, 70, 166–173, https://doi.org/10.1016/j.ocemod.2013.05.012, 2013.

Dumont, D., Kohout, A. L., and Bertino, L.: A wave-based model for the marginal ice zone including a floe breaking parameterization, J. Geophys. Res., 116, 1–12, https://doi.org/10.1029/2010JC006682, 2011.

Feltham, D. L.: Granular flow in the marginal ice zone, Philosophical Transactions of the Royal Society of London A: Mathematical, Physical and Engineering Sciences, 363, 1677–1700, 2005.

Girard, L., Bouillon, S., Weiss, J., Amitrano, D., Fichefet, T., and Legat, V.: A new modeling framework for sea-ice mechanics based on elasto-brittle rheology, Annals of Glaciology, 52, 123–132, https://doi.org/10.3189/172756411795931499, 2011.

Herman, A.: Wave-Induced Surge Motion and Collisions of Sea Ice Floes: Finite-Floe-Size Effects, Journal of Geophysical Research: Oceans, 123, 7472–7494, 2018.

Herman, A., Evers, K.-U., and Reimer, N.: Floe-size distributions in laboratory ice broken by waves, The Cryosphere, 12, 685–699, 2018.

Horvat, C. and Tziperman, E.: A prognostic model of the sea ice floe size and thickness distribution, The Cryosphere, 9, 2119–2134, https://doi.org/10.5194/tc-9-2119-2015, 2015.

Horvat, C., Tziperman, E., and Campin, J.-M.: Interaction of sea ice floe size, ocean eddies, and sea ice melting, Geophysical Research Letters, 43, 2016GL069 742, https://doi.org/10.1002/2016GL069742, 2016.

Horvat, C., Roach, L., Tilling, R., Bitz, C., Fox-Kemper, B., Guider, C., Hill, K., Ridout, A., and Sheperd, A.: Estimating The Sea Ice Floe Size Distribution Using Satellite Altimetry: Theory, Climatology, and Model Comparison, The Cryosphere Discussions, 2019, 1–25, https://doi.org/10.5194/tc-2019-134, https://www.the-cryosphere-discuss.net/tc-2019-134/, 2019.

Hwang, B., Ren, J., McCormack, S., Berry, C., Ben Ayed, I., Graber, H., and Aptoula, E.: A practical algorithm for the retrieval of floe size distribution of Arctic sea ice from high-resolution satellite Synthetic Aperture Radar imagery, Elementa, 5, https://doi.org/10.1525/elementa.154, 2017.

Johannessen, O. M., JOHANNESSEN, J. A., Morison, J., FARRELLY, B. A., and SVENDSEN, E. A. S.: Oceanographic Conditions in the Marginal Ice Zone North of Svalbard in Early Fall 1979 With an Emphasis on Mesoscale Processes, J. Geophys. Res., 88, 2755–2769, 1983.

Kaleschke, L., Lüpkes, C., Vihma, T., Haarpaintner, J., Hartmann, A. B. J., and Heygster, G.: SSM/I Sea ice remote sensing for mesoscale ocean-atmospheres, Canadian J. Remote Sensing, 27, 526–537, 2001.

Kohout, A. L. and Meylan, M. H.: An elastic plate model for wave attenuation and ice floe breaking in the marginal ice zone, J. Geophys. Res., 113, doi:10.1029/2007JC004 434, 2008.

Kohout, A. L., Williams, M. J. M., Toyota, T., Lieser, J., and Hutchings, J. K.: In situ observations of wave-induced ice floe breakup, Deep-Sea Res. II, 131, 22–27, https://doi.org/10.1016/j.dsr2.2015.06.010, 2016.

Langhorne, P. J., Squire, V. A., Fox, C., and Haskell, T. G.: Break-up of sea ice by ocean waves, Annals of Glaciology, 27, 438–442, 1998.

Lemieux, J.-F., Dupont, F., Blain, P., Roy, F., Smith, G. C., and Flato, G. M.: Improving the simulation of landfast ice by combining tensile strength and a parameterization for grounded ridges, Journal of Geophysical Research: Oceans, 121, 7354–7368, https://doi.org/10.1002/2016JC012006, https://agupubs.onlinelibrary.wiley.com/doi/abs/10.1002/2016JC012006, 2016.

Longuet-Higgins, M. S.: The Mean Forces Exerted by Waves on Floating or Submerged Bodies with Applications to Sand Bars and Wave Power Machines, Proceedings of the Royal Society of London. A. Mathematical and Physical Sciences, 352, 463–480, https://doi.org/10.1098/rspa.1977.0011, http://rspa.royalsocietypublishing.org/content/352/1671/463.abstract, 1977.

Madec, G.: NEMO ocean engine, Note du Pôle de modélisation, Institut Pierre-Simon Laplace (IPSL), France, No 27, ISSN No 1288-1619, 2008.

https://doi.org/10.5194/tc-2020-19
Preprint. Discussion started: 24 January 2020

Manucharyan, G. E. and Thompson, A. F.: Submesoscale sea ice-ocean interactions in marginal ice zones, Journal of Geophysical Research: Oceans, 122, 9455–9475, 2017.

McPhee, M. G.: An analysis of pack ice drift in summer, Sea ice processes and models, pp. 62–75, 1980.

Meier, W. N.: Losing Arctic sea ice: Observations of the recent decline and the long-term context, in: Sea Ice, edited by Thomas, D. N., chap. 11, pp. 290–303, John Wiley & Sons, 3 edn., 2017.

Mellor, M.: The Mechanics of Sea Ice, in: The Geophysics of Sea Ice, edited by Untersteiner, N., pp. 165–182, 1986.

Montiel, F. M. and Squire, V. A.: Modelling wave-induced sea ice breakup in the marginal ice zone, Proc. R. Soc. A, 473, https://doi.org/10.1098/rspa.2017.0258, 2017.

Mosig, J., Montiel, F. M., and Squire, V.: Comparison of viscoelastic-type models for ocean wave attenuation in ice-covered seas, J. Geophys. Res., https://doi.org/10.1002/ 2015JC010881, 2015.

Oikkonen, A., Haapala, J., Lensu, M., Karvonen, J., and Itkin, P.: Small-scale sea ice deformation during N-ICE2015: From compact pack ice to marginal ice zone, Journal of Geophysical Research: Oceans, 122, 5105–5120, 2017.

Rampal, P., Bouillon, S., Ólason, E., and Morlighem, M.: neXtSIM: a new Lagrangian sea ice model, The Cryosphere, 10, 1055–1073, https://doi.org/10.5194/tc-10-1055-2016, 2016.

Rampal, P., Dansereau, V., Óláson, E., Williams, T. D., and Samaké, A.: On the multi-fractal scaling properties of sea ice deformation, The Cryosphere, 13, 2457–2474, https://doi.org/10.5194/tc-13-2457-2019, https://www.the-cryosphere.net/13/2457/2019/, 2019.

Roach, L. A., Horvat, C., Dean, S. M., and Bitz, C. M.: An emergent sea ice floe size distribution in a global coupled ocean–sea ice model, Journal of Geophysical Research: Oceans, 2018.

Rothrock, D. and Thorndike, A.: Measuring the sea ice floe size distribution, Journal of Geophysical Research: Oceans, 89, 6477–6486, 1984.

Rousset, C., Vancoppenolle, M., Madec, G., Fichefet, T., Flavoni, S., Barthélemy, A., Benshila, R., Chanut, J., Lévy, C., Masson, S., et al.: The Louvain-La-Neuve sea ice model LIM3. 6: global and regional capabilities, Geoscientific Model Development, 8, 2991, 2015.

Saha, S., Moorthi, S., Wu, X., Wang, J., Nadiga, S., Tripp, P., Behringer, D., Hou, Y.-T., Chuang, H.-y., Iredell, M., Ek, M., Meng, J., Yang, R., Mendez, M. P., van den Dool, H., Zhang, Q., Wang, W., Chen, M., and Becker, E.: The NCEP Climate Forecast System Version 2, Journal of Climate, 27, 2185–2208, https://doi.org/10.1175/JCLI-D-12-00823.1, https://doi.org/10.1175/JCLI-D-12-00823.1, 2014.

Sakov, P., Counillon, F., Bertino, L., Lisæter, K. A., Oke, P. R., and Korablev, A.: TOPAZ4: an ocean-sea ice data assimilation system for the North Atlantic and Arctic, Ocean Science, 8, 633–656, 2012.

Shen, H. H., Hibler, W. D., and Leppäranta, M.: On Applying Granular Flow Theory to a Deforming Broken Ice Field, Acta Mechanica, 63, 143–160, 1986.

Spreen, G., Kaleschke, L., and Heygster, G.: Sea ice remote sensing using AMSR-E 89-GHz channels, Journal of Geophysical Research: Oceans, 113, 2008.

Squire, V. A.: Of Ocean Waves and Sea-Ice Revisited, Cold Regions Science and Technology, 49, 110–133, 2007.

Squire, V. A.: Past, present and impendent hydroelastic challenges in the polar and subpolar seas, Phil. Trans. R. Soc. Lond. A., 369, 2813—2831, https://doi.org/10.1098/rsta.2011.0093, 2012.

Squire, V. A.: Ocean Wave Interactions with Sea Ice: A Reappraisal, Annual Review of Fluid Mechanics, 52, null, https://doi.org/10.1146/annurev-fluid-010719-060301, 2020.

Squire, V. A., Dugan, J. P., Wadhams, P., Rottier, P. J., and Liu, A. J.: Of Ocean Waves and Sea Ice, Annu. Rev. Fluid Mech., 27, 115–168, 1995.

https://doi.org/10.5194/tc-2020-19
Preprint. Discussion started: 24 January 2020

Steele, M.: Sea Ice Melting and Floe Geometry in a Simple Ice-Ocean Model, J. Geophys. Res., 97, 17 729–17 738, 1992.

Stopa, J., Ardhuin, F., and Girard-Ardhuin, F.: Wave climate in the Arctic 1992-2014: Seasonality and trends, The Cryosphere, 10, 1605–1629, 2016.

Stopa, J., Ardhuin, F., Thomson, J., Smith, M. M., Kohout, A., Doble, M., and Wadhams, P.: Wave Attenuation Through an Arctic Marginal Ice Zone on 12 October, 2015: 1. Measurement of Wave Spectra and Ice Features From Sentinel-1A, Journal of Geophysical Research: Oceans, 2018a.

Stopa, J. E., Sutherland, P., and Ardhuin, F.: Strong and highly variable push of ocean waves on Southern Ocean sea ice, Proceedings of the National Academy of Sciences, 115, 5861–5865, 2018b.

Sutherland, P. and Dumont, D.: Marginal ice zone thickness and extent due to wave radiation stress, Journal of Physical Oceanography, 48, 1885–1901, 2018.

The WAVEWATCH III Development Group: User manual and system documentation of WAVEWATCH III version 6.07, Tech. Rep. 333, Environmental Modeling Center Marine Modeling and Analysis Branch, 2019.

Thomson, J. and Rogers, W. E.: Swell and sea in the emerging Arctic Ocean, Geophys. Res. Lett., 41, 3136–3140, https://doi.org/10.1002/2014GL059983, 2014.

Thomson, J., Ackley, S., Girard-Ardhuin, F., Ardhuin, F., Babanin, A., Bidlot, J., Boutin, G., Brozena, J., Cheng, S., Doble, M., et al.: Overview of the arctic sea state and boundary layer physics program, Journal of Geophysical Research: Oceans, 2018.

Tietsche, S., Day, J., Guemas, V., Hurlin, W., Keeley, S., Matei, D., Msadek, R., Collins, M., and Hawkins, E.: Seasonal to interannual Arctic sea ice predictability in current global climate models, Geophysical Research Letters, 41, 1035–1043, 2014.

Toyota, T., Haas, C., and Tamura, T.: Size distribution and shape properties of relatively small sea-ice floes in the Antarctic marginal ice zone in late winter, Deep-Sea Res. II, 58, 1182–1193, 2011.

Williams, T. D., Bennetts, L. G., Squire, V. A., Dumont, D., and Bertino, L.: Wave-ice interactions in the marginal ice zone. Part 1: Theoretical foundations, Ocean Modelling, 71, 81–91, https://doi.org/10.1016/j.ocemod.2013.05.010, 2013a.

Williams, T. D., Bennetts, L. G., Squire, V. A., Dumont, D., and Bertino, L.: Wave-ice interactions in the marginal ice zone. Part 2: Numerical implementation and sensitivity studies along 1D transects of the ocean surface, Ocean Modelling, 71, 92–101, https://doi.org/10.1016/j.ocemod.2013.05.011, 2013b.

Williams, T. D., Rampal, P., and Bouillon, S.: Wave-ice interactions in the neXtSIM sea-ice model, The Cryosphere, 11, 2117–2135, https://doi.org/10.5194/tc-11-2117-2017, 2017.

Zhang, J., Shweiger, A., Steele, M., and Stern, H.: Sea ice floe Size Distribution in the Marginal Ice Zone: Theory and Numerical Experiments, J. Geophys. Res., https://doi.org/DOI 10.1002/2015JC010770, 2015.

Zhang, J., Stern, H., Hwang, B., Schweiger, A., and Steele, M.: Modeling the seasonal evolution of the Arctic sea ice floe size distribution., Elem Sci Anth, 4, https://doi.org/10.12952/journal.elementa.000126, 2016.

https://doi.org/10.5194/tc-2020-19
Preprint. Discussion started: 24 January 2020

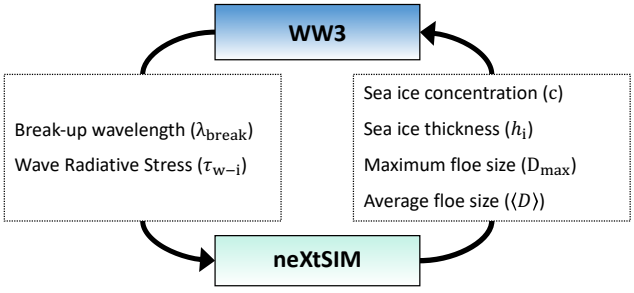

Figure 1. Summary of the exchanged variables in the neXtSIM-WW3 coupling framework.

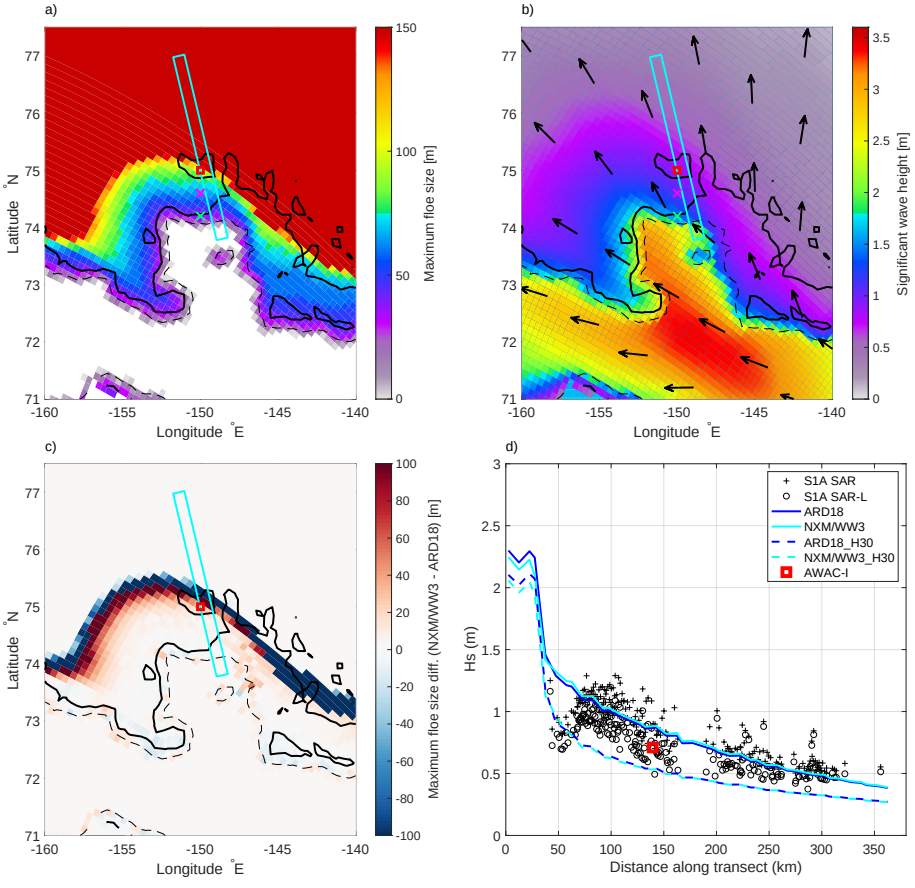

Figure 2. Spatial distributions of maximum floe size (a) and significant wave height (b) in the Beaufort Sea taken from the NXM/WW3 simulation on 12th October at 17:00:00 GMT. The difference of the maximum floe size distribution with the ARD18 simulation is shown on (c). Evolution of the significant wave height for different simulations along the transect depicted in cyan on panels (a,b,c) is presented on panel (d), along with significant wave height estimated from Sentinel-1a SAR images (see Stopa et al., 2018a; Ardhuin et al., 2018, for details) and measured by an AWAC buoy. The AWAC position is depicted by a red square on panels (a,b,c). The green and magenta crosses indicate the position at which are shown the FSD on Figure 3.

https://doi.org/10.5194/tc-2020-19
Preprint. Discussion started: 24 January 2020

The Cryosphere
Discussions
Open Access
EGU

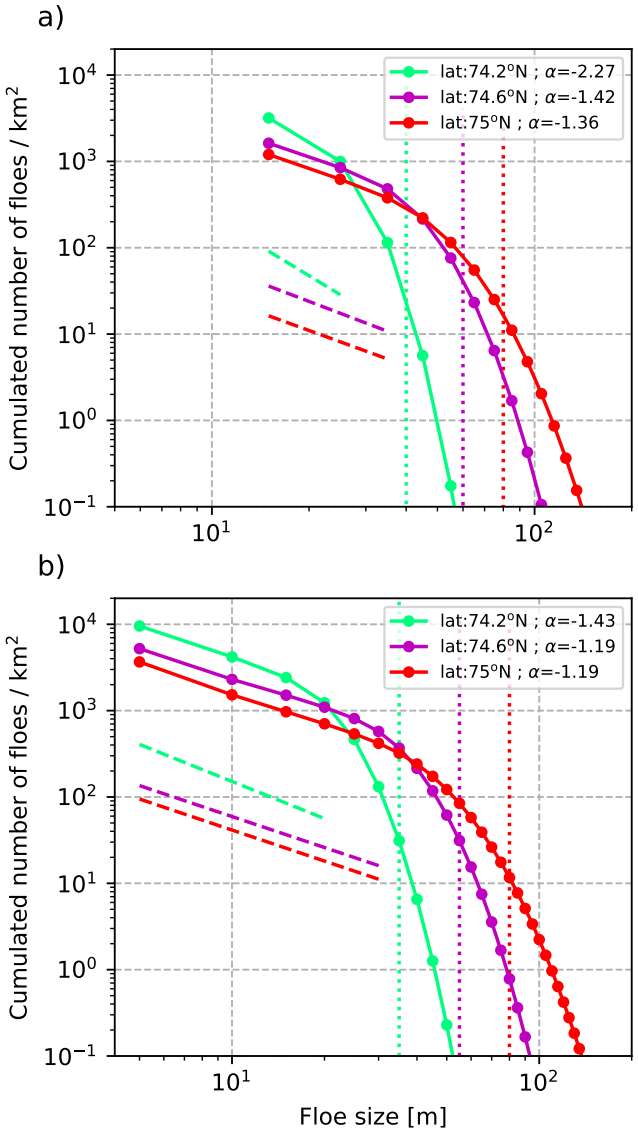

Figure 3. Cumulated distribution of floes taken at three different locations from the NXM/WW3 simulation (a), and from the NXM/WW3_refine simulation (b). The three locations share the same longitude (150°W) and their position is indicated by a symbol of the same color in Fig. 2(a,b) (red colour corresponds to the AWAC position). The dashed lines correspond to the linear regression over the smallest floe size categories for each location. Values of the slope α are given in the legend. The vertical dotted lines represent the $D_{\max}$ values for each case.

https://doi.org/10.5194/tc-2020-19
Preprint. Discussion started: 24 January 2020

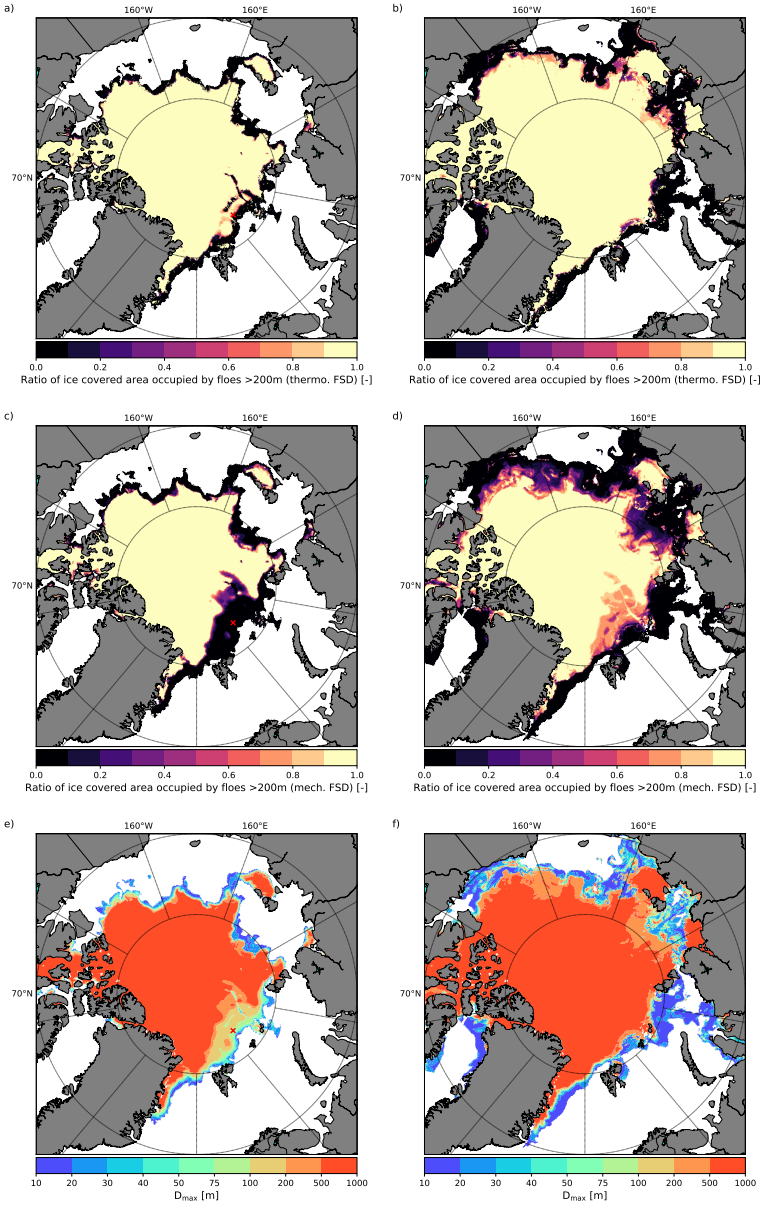

Figure 4. Pan-Arctic distribution of the area covered by floes with diameters larger than 200 m over the total sea ice cover area according to the 'thermodynamical' (a,b) FSD and to the 'mechanical' FSD (c,d), as well as the distribution of the maximum floe size (e,f). Each column corresponds to a different time: 02/10/2015 00:00:00 (a,c,e) and 01/11/2015 00:00:00 (b,c,f). The cross indicates the location at which the FSDs shown on Figure 5 are taken.

https://doi.org/10.5194/tc-2020-19
Preprint. Discussion started: 24 January 2020

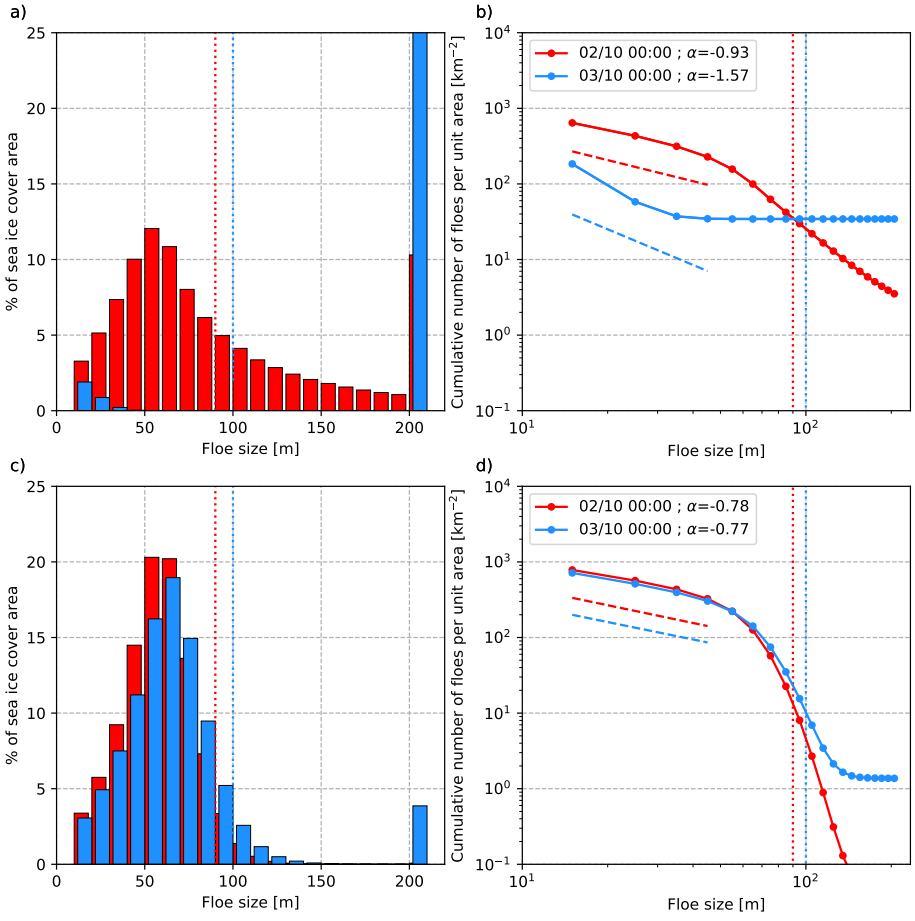

Figure 5. Areal (a,c) and cumulated distribution of floes (b,d) for the thermodynamical (a,b) and mechanical (c,d) FSDs taken at 45°E and 83.5°N. Each color refers to a different time: 02/10/2015 00:00:00 (red) and 03/10/2015 00:00:00 (blue). The dashed lines correspond to the linear regression over the smallest floe size categories for each location. Values of the slope α are given in the legend. The vertical dotted lines represent the $D_{\max}$ values for each date.

https://doi.org/10.5194/tc-2020-19
Preprint. Discussion started: 24 January 2020

The Cryosphere
Discussions
Open Access
EGU

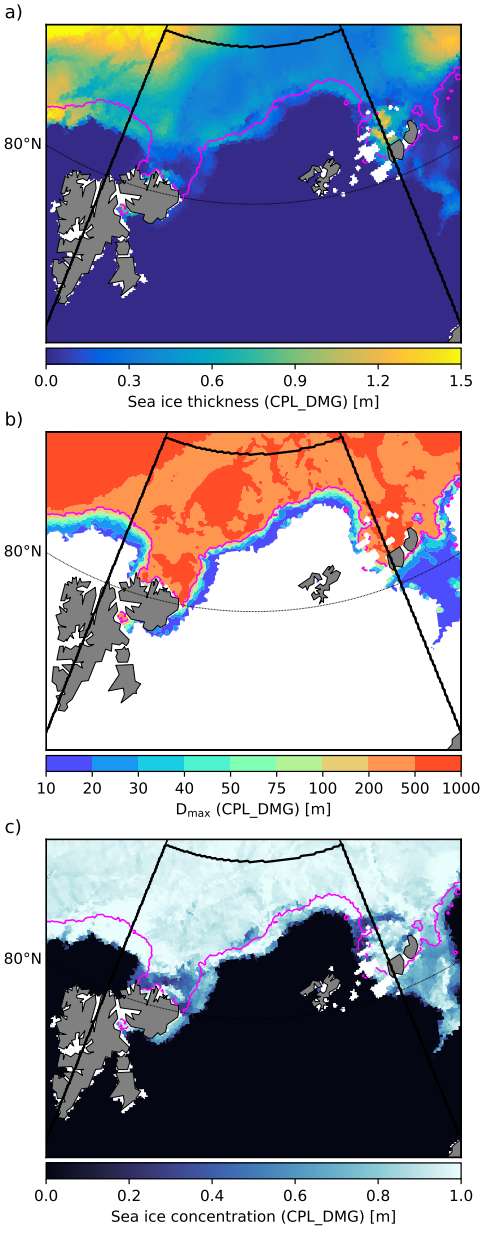

Figure 6. Distributions of sea ice thickness (a), maximum floe size (b) and sea ice concentration from the CPL_DMG simulation in the Barents sea on October 15$^{\text{th}}$ 2015, at 00:00:00. The magenta line corresponds to the contour $D_{\max} = 200$ m in CPL_DMG. The black thick lines delimit the domain used to analyse results from the 3 simulations (REF, CPL_WRS, CPL_DMG) in figures 7, 10 and 13.

https://doi.org/10.5194/tc-2020-19
Preprint. Discussion started: 24 January 2020

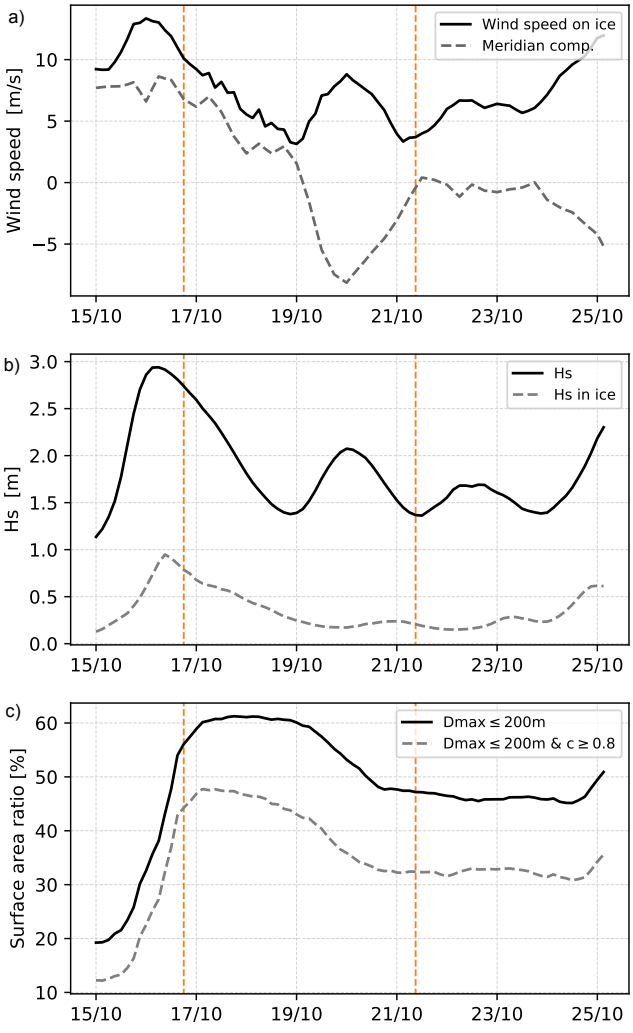

Figure 7. Temporal evolution of (a) the wind speed (black solid line) and its meridian component (dashed grey line) averaged over all the ice-covered part of the domain (see Fig. 6 for the domain definition), (b) the significant wave height averaged over all the domain (black solid line) and ice-covered part of the domain only (dashed grey line), and (c) the ratio of the surface area of regions covered by recently broken sea ice (defined as $D_{\max} \leq 200$ m, black solid line) and compact sea ice that has been recently broken (defined as $D_{\max} \leq 200$ m and $c \geq 0.8$, grey dashed line) over the total sea ice-covered surface area. The time period shown covers from October 15$^{\text{th}}$ to October 25$^{\text{th}}$ 2015, for which initial conditions are given in Figure 6. The sea ice-covered part of the domain is the area for which the sea ice concentration c is greater than 0. The two orange vertical lines indicates the dates of the snapshots shown in Figures 8, 9 and 11.

https://doi.org/10.5194/tc-2020-19
Preprint. Discussion started: 24 January 2020

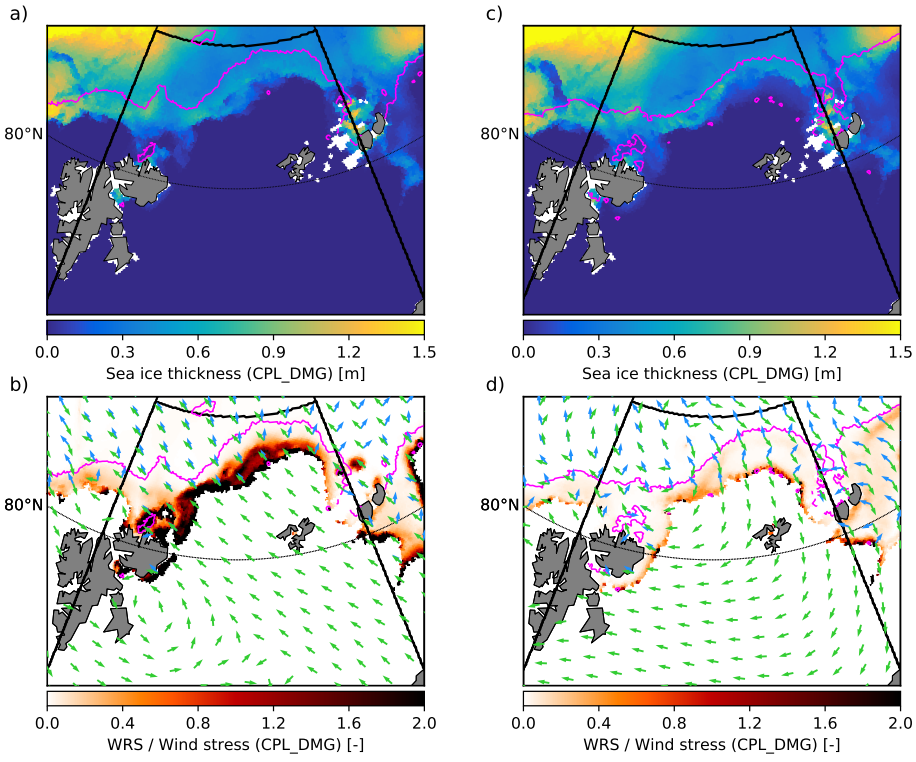

Figure 8. Snapshots of the distributions of sea ice thickness (a,c), and of the ratio between the WRS and the wind stress over sea ice (b,d) from the CPL_DMG simulation in the Barents sea taken on October 16$^{\mathrm{th}}$ 2015 at 18:00:00 GMT (a,b), and on October 21$^{\mathrm{st}}$ 2015 at 09:00:00 GMT (c,d). The wind and WRS directions for each date are given by the green and blue arrows respectively on panels (b,d). The magenta line corresponds to the contour $D_{\mathrm{max}} = 200$ m in CPL_DMG. The black thick lines delimit the domain used to analyse results from the 3 simulations (REF, CPL_WRS, CPL_DMG) in Figures 7, 10 and 13.

https://doi.org/10.5194/tc-2020-19
Preprint. Discussion started: 24 January 2020

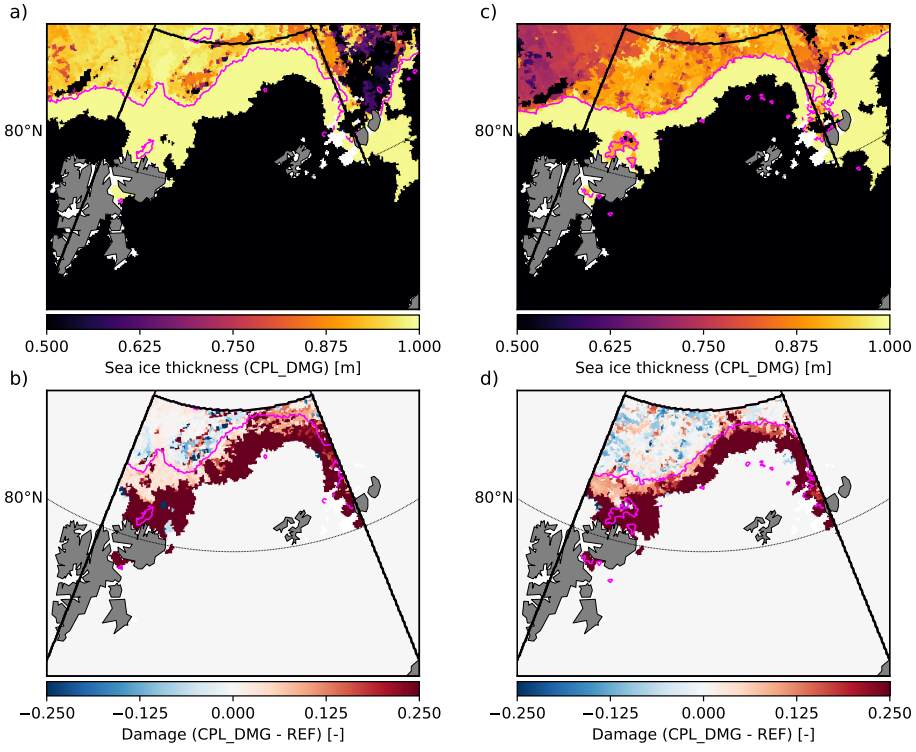

Figure 9. Snapshots of the distributions of sea ice damage in the CPL_DMG simulation (a,c), and of the differences in damage between the CPL_DMG and REF simulations (b,d) in the Barents sea taken on October 16$^{\text{th}}$ 2015 at 18:00:00 GMT (a,b), and on October 21$^{\text{st}}$ 2015 at 09:00:00 GMT (c,d). The wind and WRS directions for each date are given by the green and blue arrows respectively on panels (b,d). The magenta line corresponds to the contour $D_{\max} = 200$ m in CPL_DMG. The black thick lines delimit the domain used to analyse results from the 3 simulations (REF, CPL_WRS, CPL_DMG) in Figures 7, 10 and 13.

https://doi.org/10.5194/tc-2020-19
Preprint. Discussion started: 24 January 2020

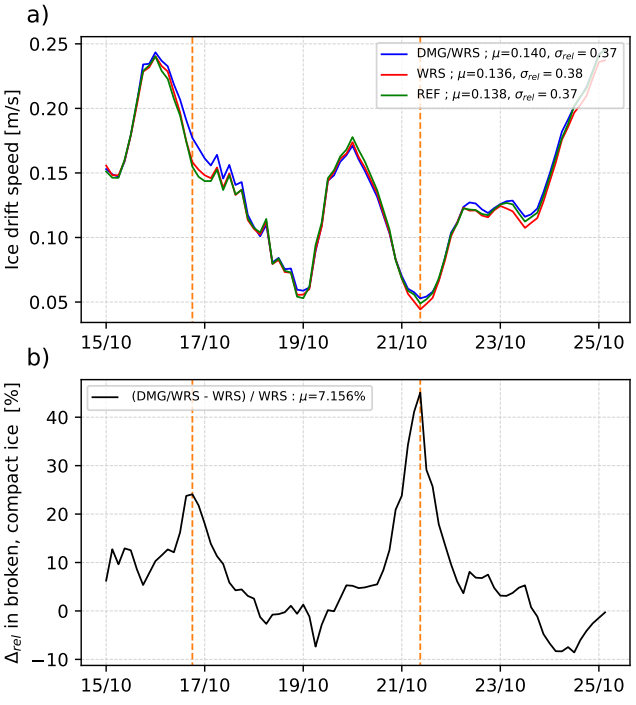

Figure 10. Temporal evolution of (a) the ice drift velocity averaged over all the ice-covered part of the domain (see Fig. 6 for the domain definition) for the three simulations (REF in green, CPL_WRS in red, and CPL_DMG in blue), and (b) the difference of ice drift velocity in the region covered by compact sea ice that has been recently broken (defined as $D_{\max} \leq 200\,\mathrm{m}$ and $c \geq 0.8$) between the CPL_WRS and CPL_DMG simulations. The time period shown covers from October 15$^{\mathrm{th}}$ to October 25$^{\mathrm{th}}$ 2015, for which initial conditions are given in Figure 6. The sea ice-covered part of the domain corresponds to the area for which the sea ice concentration c is greater than 0. The two orange vertical lines indicates the dates of the snapshots shown in Figures 8, 9 and 11. In the panels legends, μ indicates the temporal mean associated with each curve, and σ_{rel} is the standard deviation divided by the mean.

https://doi.org/10.5194/tc-2020-19
Preprint. Discussion started: 24 January 2020

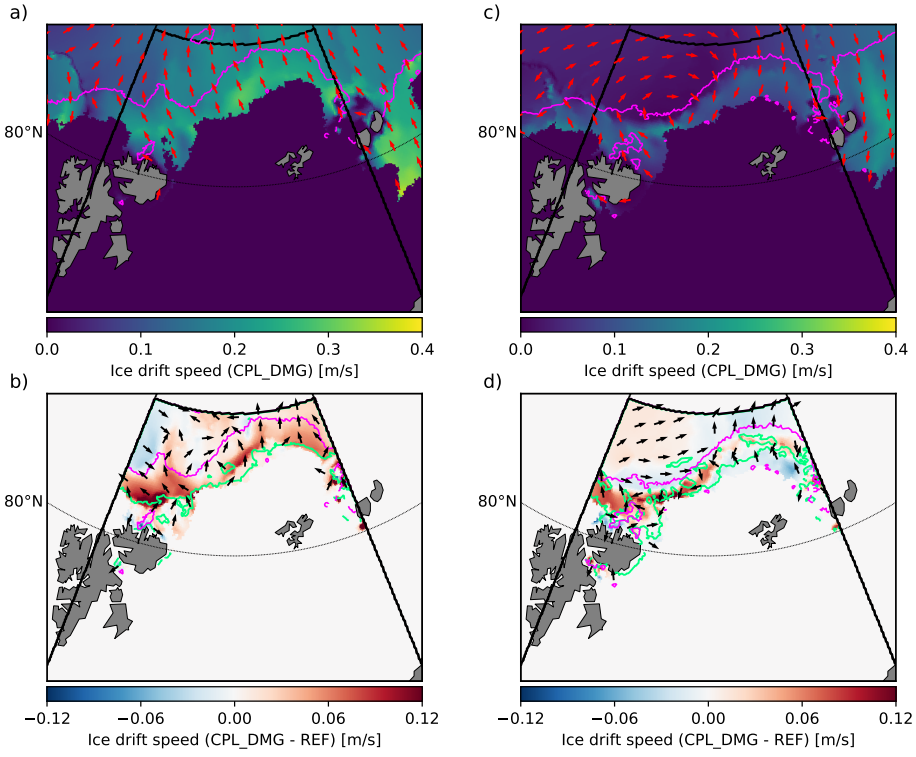

Figure 11. Snapshots of the distributions of sea ice drift velocity in the CPL_DMG simulation (a,c), and of the differences in sea ice drift velocity between the CPL_DMG and REF simulations (b,d) in the Barents sea taken on October 16$^{\mathrm{th}}$ 2015 at 18:00:00 GMT (a,b), and on October 21$^{\mathrm{st}}$ 2015 at 09:00:00 GMT (c,d). The green line delimits the area with compact sea ice (defined as $c \geq 0.8$) in CPL_DMG. The magenta line corresponds to the contour $D_{\mathrm{max}} = 200$ m in CPL_DMG. The black thick lines delimit the domain used to analyse results from the 3 simulations (REF, CPL_WRS, CPL_DMG) in Figures 7, 10 and 13.

https://doi.org/10.5194/tc-2020-19
Preprint. Discussion started: 24 January 2020

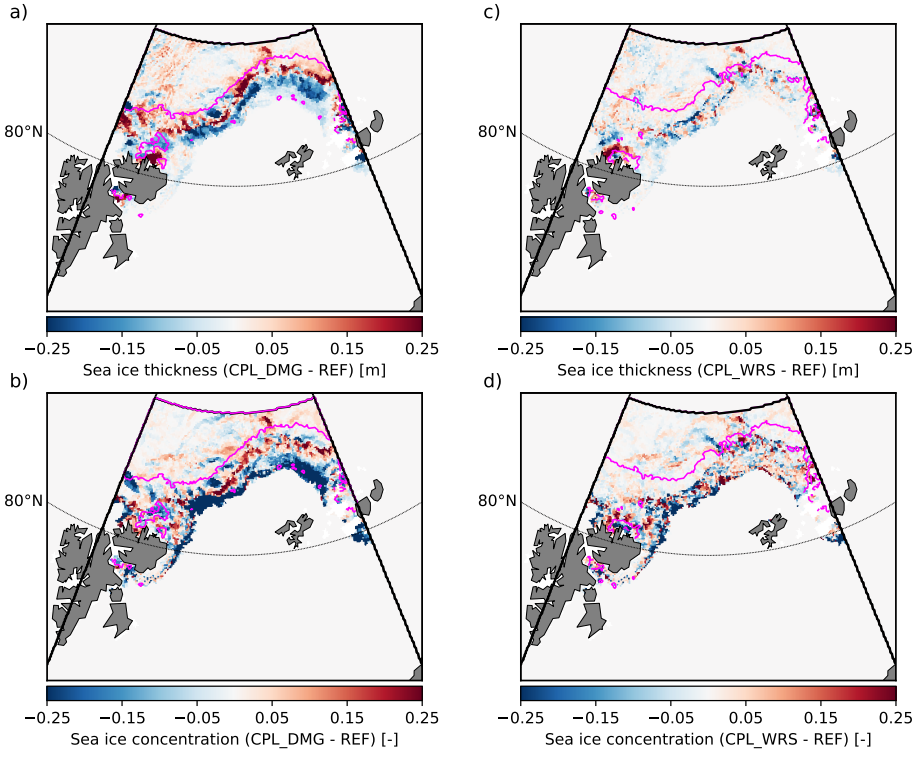

Figure 12. Snapshots of the distributions of difference in sea ice thickness (a,c) and sea ice concentration (b,d) between the CPL_DMG and the REF simulations (a,b), and between the CPL_WRS and REF simulations (c,d). All these snapshots are taken on October 21st 2015 at 09:00:00 GMT. The magenta line corresponds to the contour $D_{\max} = 200$ m in CPL_DMG (a,b) and in CPL_WRS (c,d). The black thick lines delimit the domain used to analyse results from the 3 simulations (REF, CPL_WRS, CPL_DMG) in Figures 7, 10 and 13.

https://doi.org/10.5194/tc-2020-19
Preprint. Discussion started: 24 January 2020

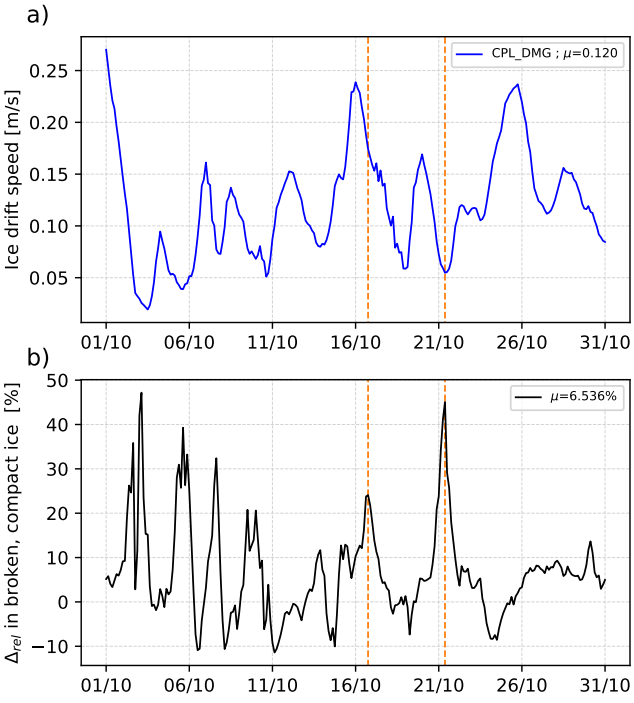

Figure 13. Temporal evolution of (a) the ice drift velocity averaged over all the ice-covered part of the domain (see Fig. 6 for the domain definition) for the CPL_DMG simulation, over October 2015, and (b) of the difference of ice drift velocity in the region covered by compact sea ice that has been recently broken (defined as $D_{\max} \leq 200$ m and $c \geq 0.8$) between the CPL_WRS and CPL_DMG simulations. The sea ice-covered part of the domain corresponds to the area for which the sea ice concentration c is greater than 0. The two orange vertical lines indicates the dates of the snapshots shown in Figures 8, 9 and 11. In each panel legend, μ indicates the temporal mean of the plotted quantity.